Hyperfine Interactions 123/124 (1999) 681–719

Polarization effects in resonant nuclear scattering

D.P. Siddons [a], U. Bergmann [b] and J.B. Hastings [a]

[a] *National Synchrotron Light Source, Brookhaven National Laboratory, Upton, NY 11973, USA*
[b] *Physical Biosciences Division, Lawrence Berkeley National Laboratory, Berkeley, CA 94720, USA*

Polarization phenomena are present in every radiative transition, whether it is of atomic or nuclear origin. Nuclear resonant scattering of synchrotron radiation is an ideal technique for their study because (a) the probing radiation is in a well characterized polarization state, in most cases linear, (b) the scattered radiation can be efficiently analyzed with polarization filters, and (c) synchrotron pulses are very short compared to the lifetime of a nuclear resonance, resulting in a clean signal. In the following article we describe experimental and theoretical studies of the 14.4 keV Mössbauer resonance of ^{57}Fe and its transitions with linear and circular polarization. After introducing the required instrumentation a formalism to calculate time dependent polarization phenomena is derived. With the help of different scattering geometries we illustrate various aspects, such as polarization mixing and selective excitation of subsets of the resonance. Perhaps the most fascinating example is the Faraday geometry where the E-vector rotates several 360° turns during the lifetime of the resonant scattering. A comparison of this phenomenon with the optical Faraday effect is given. New powerful synchrotron radiation sources will enable researchers to exploit polarization phenomena in nuclear resonant scattering to detect subtle changes in physically and chemically relevant systems.

1. Introduction

1.1. X-ray polarization phenomena

Some of the most intriguing phenomena in the field of nuclear resonance scattering are associated with the polarization properties of the different transitions. In this chapter we will outline a formalism for describing these phenomena, and describe some of the experiments which illustrate their richness.

Polarization phenomena in the visible region of the spectrum are easily studied, and applications are now commonplace. The situation in the X-ray spectral region is quite different. The search for evidence of optical activity in the X-ray region has only recently been successful [1], primarily because all early X-ray studies were performed at one of the fixed wavelengths generated by X-ray tubes. Optical activity (and we use this term loosely to include all polarization phenomena) is essentially a resonance phenomenon, and resonances in the X-ray region are sufficiently narrow that these fixed wavelengths produced negligible activity. This situation changed dramatically with the introduction of powerful synchrotron radiation (SR) sources, which allowed a free choice of energy, and hence access to core electron resonances. X-ray polar-

ization phenomena based on electronic resonances are not significantly different from their optical counterparts, since typical resonance widths in atomic X-ray spectra are of order 1 eV wide. Consequently, the lifetimes of the excited states are very short. Thus, one always observes their time-integrated behavior. Nuclear resonances, in contrast, are very sharp, and the excited states live long enough for us to observe their time-dependent behavior. The energy differences between the hyperfine-split lines are comparable to or greater than their width, and each transition has a definite polarization. The incident SR pulse excites all levels which its polarization will allow it to couple to in a coherent fashion. The interference among the emission lines from the decay produces an instantaneous polarization which is time-dependent on the nanosecond time scale. A full description of the phenomena would require us to consider partially polarized incident light, see, e.g., Blume and Kistner [2]. Blume was studying the scattering of a radioactive source by a magnetic sample, therefore, the Poincaré representation was essential. Since SR is almost completely linearly polarized, we choose to adopt the Jones formalism, which makes the treatment significantly simpler (see, e.g., [3]). In particular, the Jones formalism in a linear polarization basis is appropriate. Although the standard Jones description applies for systems having constant matrices (i.e., frequency-independent matrix elements), in the following, we will extend it to include the case of scattering by hyperfine-split nuclear resonances.

1.2. X-ray polarimetry

The fact that X-rays are polarized was recognized along with the recognition of their nature as electromagnetic waves, and experimentalists since Barkla have worked on this aspect of X-rays. The weak X-ray interaction with matter prevented the development of efficient X-ray polarizers and analyzers until highly perfect semiconductor crystal materials became readily available. The use of perfect-crystal Bragg reflection polarizers was pioneered by Hart [4], who demonstrated that extremely high extinction ratios could be attained in a simple polarimeter consisting of crossed linear polarizers. His earliest experiments used Cu Kα radiation from a standard X-ray tube and the (3 3 3) Bragg reflection from germanium. This combination of reflection and wavelength resulted in a Bragg angle of almost exactly 45°. Thus, only σ-polarized radiation was reflected. Hart's polarimeter consisted of two monolithic devices, each providing two consecutive Bragg reflections, with the diffraction planes orthogonal, in analogy with the "crossed polarizers" of conventional optics. Such a multiple-reflection monolithic device is commonly referred to as a "channel-cut" monochromator [5]. In addition to conveniently bringing the monochromatic (and polarized) beam back to the same direction as the incident beam, the second reflection serves to enhance the polarizing effectiveness of the device. This instrument was, however, a fixed wavelength device, and it was only when the extension of the technique to provide a tunable device was made [6] that the door was opened to resonant scattering phenomena (both electronic and nuclear). The tunable polarimeter relies on the fact that the dynamical reflection curve has a total-reflection region whose width depends on the polarization

of the radiation being Bragg reflected. Near Bragg angles of 45°, the width of the π reflection curve approaches zero. Thus, if, instead of two perfectly-aligned Bragg reflections in our channel-cut crystal, a slight misorientation is deliberately introduced, then the π reflection curves will not overlap, while the σ curves may still do so if the misorientation is correctly chosen. In their paper, Hart and Rodrigues [6] show how to achieve polarization ratios of better than 10^5 over a wide energy range by a suitable choice of reflection and offset. A pair of such devices was used to demonstrate the X-ray Faraday effect [7] arising from electronic resonances near X-ray absorption edges in magnetic materials. Fortunately, for nuclear resonant scattering from ^{57}Fe there is one reflection in silicon which has a Bragg angle of 45.1°, the (8 4 0) reflection. This is quite a high diffraction order and so it has a rather narrow reflectivity curve. In order to enhance this characteristic, it is possible to use asymmetric reflections, in which the crystal surface is not parallel to the Bragg planes. The larger the asymmetry, the more the reflection width is enhanced. However, there are problems if this technique is taken to extremes. Our experience has been that an asymmetry factor (the ratio of the incident and reflected beam direction cosines) of around 10 is optimal. It does not demand extremely smooth surfaces, nor require the ultimate in crystal perfection in order to work as expected. The monochromator we developed for the experiments described here used a combination of symmetric and asymmetric reflections so as to enhance the reflection width and polarization properties and also reduce the energy passband of the device [8]. Figure 1 shows the calculated reflectivity curve for this 4-reflection asymmetric–symmetric dispersive monochromator. The corresponding

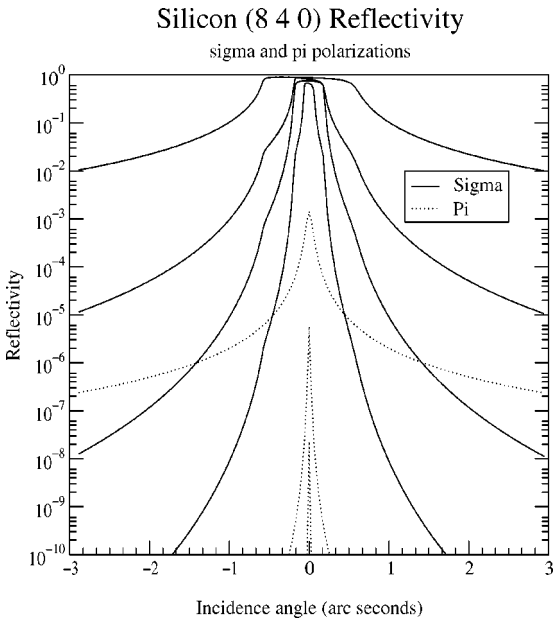

Figure 1. The calculated reflectivity curves for the σ and π polarizations at various points throughout the 4-reflection Si(8 4 0) monochromator illustrated in figure 2.

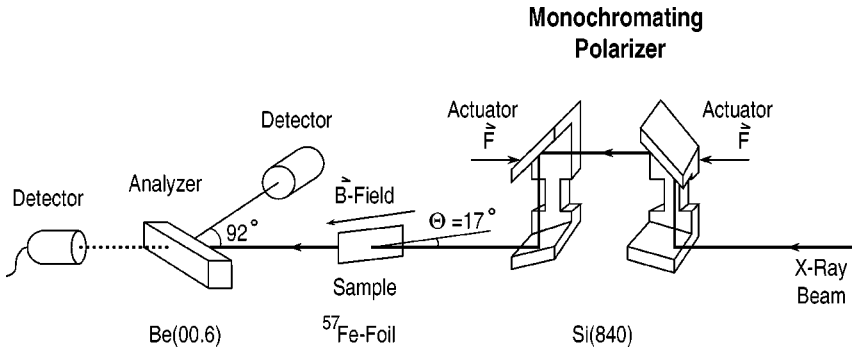

Figure 2. The experimental arrangement used for measurements with a bending-magnet source at NSLS. The 4-reflection monochromator provides an energy resolution of around 10 meV and a polarization ratio of better than 10^6.

geometry is illutrated in figure 2. The analyzer we used depended on the details of the synchrotron source available. All of our early experiments were performed using a dipole source at the National Synchrotron Light Source (NSLS). Using this source, the horizontal divergence of the X-ray beam was quite large compared to even the enhanced reflection width of the (8 4 0) reflection. Our compromise consisted of using a mosaic crystal as an analyzer, having a mosaic spread of a few arc minutes (compared to around 1 arc second for the silicon). The beryllium (0 0 0.6) reflection has a Bragg angle of 46°; not perfect but close enough to demonstrate some of the principles involved. For our experiments using third generation undulator sources [9], we used the silicon device as both monochromator and analyzer, with significantly enhanced performance and a quite acceptable throughput. Other authors have used similar devices to achieve a similar performance [10]. It is clearly possible, with care, to achieve suppression of σ–σ scattering by factors of 10^6 or better using such techniques, a fact which will allow nuclear forward scattering (NFS) experiments on oriented hyperfine-split samples with much greater ease and accuracy, since the experiment will no longer be detector-limited by the huge prompt burst of nonresonant scattering.

In the following sections we will first outline a simple theoretical approach based on Jones matrices which will permit the straightforward calculation of an arbitrary sequence of optical elements and samples, and then go on to consider specific cases for which experimental data have been recorded.

2. Time-dependent polarization phenomena

2.1. The Jones formalism

A Jones vector represents the electric field vector in a linear basis, and can be written as

$$\mathbf{E} = \begin{bmatrix} E_\sigma(t) \\ E_\pi(t) \end{bmatrix}, \tag{2.1}$$

where $E_\pi(t)$ and $E_\sigma(t)$ are the instantaneous scalar components of **E**, and the subscripts σ and π refer to horizontal and vertical polarization respectively.[1] In the case of coherent waves eq. (2.1) can be written as

$$\mathbf{E} = \begin{bmatrix} E_{0\sigma} \mathrm{e}^{\mathrm{i}\phi_\sigma} \\ E_{0\pi} \mathrm{e}^{\mathrm{i}\phi_\pi} \end{bmatrix}, \tag{2.2}$$

where ϕ_σ and ϕ_π are the appropriate phases. Horizontal and vertical linear polarization states are thus given by

$$\mathbf{E}_\sigma = E_{0\sigma} \mathrm{e}^{\mathrm{i}\phi_\sigma} \begin{bmatrix} 1 \\ 0 \end{bmatrix} \quad \text{and} \quad \mathbf{E}_\pi = E_{0\pi} \mathrm{e}^{\mathrm{i}\phi_\pi} \begin{bmatrix} 0 \\ 1 \end{bmatrix}, \tag{2.3}$$

where the vectors referring to the polarization state are called normalized Jones vectors. For example, adding $\mathbf{E}_\sigma$ and $\mathbf{E}_\pi$ under the condition $E_{0\sigma} = E_{0\pi}$ and $\phi_\sigma = \phi_\pi$ leads to

$$\mathbf{E} = E_{0\sigma} \mathrm{e}^{\mathrm{i}\phi_\sigma} \begin{bmatrix} 1 \\ 1 \end{bmatrix}, \tag{2.4}$$

which is a linear state at $+45^\circ$. In a similar way, depending on the phase difference between the two components any other linear, elliptical or circular state can be constructed.

If a polarized incident beam represented by a Jones vector **E** passes through an optical element a new vector, $\mathbf{E}'$, emerges, which corresponds to the transmitted wave. The optical element can be described by a Jones matrix $\boldsymbol{\mathcal{J}}$ leading to

$$\mathbf{E}' = \boldsymbol{\mathcal{J}}\mathbf{E}, \tag{2.5}$$

where $\boldsymbol{\mathcal{J}}$ is a 2×2 matrix.

Table 1 shows normalized Jones vectors and matrices for different polarization states.[2] If the wave passes through a series of optical elements given by $\boldsymbol{\mathcal{J}}_1, \boldsymbol{\mathcal{J}}_2, \ldots, \boldsymbol{\mathcal{J}}_n$, eq. (2.5) can be replaced by the more general equation

$$\mathbf{E}' = \boldsymbol{\mathcal{J}}_n \cdots \boldsymbol{\mathcal{J}}_2 \boldsymbol{\mathcal{J}}_1 \mathbf{E}. \tag{2.6}$$

Obviously, representing an optical element by a Jones matrix consisting of constants is only an approximation since in practice each optical element has some frequency dependence. If the incident wave is quasi-monochromatic the frequency dependence is often negligible. This is the case for the optical elements typically used in synchrotron beamlines. Although NFS is strongly frequency dependent, the matrix $\boldsymbol{\mathcal{T}}(\omega)$,

[1] In a strict sense σ is defined as the direction perpendicular to the scattering plane and π as the direction parallel to the scattering plane. In forward scattering there is no scattering plane so σ- and π-polarization are defined in accordance to the convention used for the polarization of the SR-pulse, i.e., that the electric field vector is in the horizontal plane for σ-polarized light.

[2] The convention of circular polarization is different from that often used in optics. Right circular polarization as defined here is equivalent to positive helicity ($m = +1$), where m is the spin quantum number of the photon.

Table 1
Some selected normalized Jones vectors and matrices.

State of polarization	Jones vector	Optical element	Jones matrix
σ-polarization $\leftrightarrow$	$\begin{bmatrix}1\\0\end{bmatrix}$	σ-polarizer	$\begin{bmatrix}1&0\\0&0\end{bmatrix}$
π-polarization $\updownarrow$	$\begin{bmatrix}0\\1\end{bmatrix}$	π-polarizer	$\begin{bmatrix}0&0\\0&1\end{bmatrix}$
$+45^\circ$ polarization $\nearrow$	$\frac{1}{\sqrt{2}}\begin{bmatrix}1\\1\end{bmatrix}$	$+45^\circ$ polarizer	$\frac{1}{2}\begin{bmatrix}1&1\\1&1\end{bmatrix}$
-45° polarization $\searrow$	$\frac{1}{\sqrt{2}}\begin{bmatrix}1\\-1\end{bmatrix}$	-45° polarizer	$\frac{1}{2}\begin{bmatrix}1&-1\\-1&1\end{bmatrix}$
right circular polarization $\circlearrowright$	$\frac{1}{\sqrt{2}}\begin{bmatrix}1\\\mathrm{i}\end{bmatrix}$	right circular polarizer	$\frac{1}{2}\begin{bmatrix}1&-\mathrm{i}\\\mathrm{i}&1\end{bmatrix}$
left circular polarization $\circlearrowleft$	$\frac{1}{\sqrt{2}}\begin{bmatrix}1\\-\mathrm{i}\end{bmatrix}$	left circular polarizer	$\frac{1}{2}\begin{bmatrix}1&\mathrm{i}\\-\mathrm{i}&1\end{bmatrix}$

which represents the resonant medium, will be expressed in a form compatible with Jones matrices and vectors.

2.2. The transmission matrix $\boldsymbol{\mathcal{T}}(\omega)$

The transmission of radiation through a Mössbauer medium has been discussed by several authors (see, e.g., [2,11,12]). In the following treatment the resonant medium is desribed by an index of refraction [2]. In general, the index of refraction is a complex frequency dependent tensor $\tilde{n}(\omega)$ which accounts for optical phenomena such as birefringence, linear and circular dichroism, Faraday, Cotton-Mouton, Voigt, Kerr and Pockels effects. In this context $\tilde{n}(\omega)$ will be represented by a 2×2 matrix expressed in a linear basis. Consider the solution of the wave equation in a dispersive medium. The amplitude $\mathbf{A}'(\omega)$ of an electromagnetic wave transmitted through such a medium of thickness L is given by

$$\mathbf{A}'(\omega) = \mathrm{e}^{\mathrm{i}\tilde{n}(\omega)k_0 L}\mathbf{A}(\omega), \tag{2.7}$$

where k_0 is the wave vector in vacuum, which is related to the frequency ω of the incident wave through $k_0 = \omega/c$.

Equation (2.7) can be brought into a matrix form by expanding the exponential term. The resulting 2×2 matrix is called the transmission matrix $\boldsymbol{\mathcal{T}}(\omega)$, and eq. (2.7) can be rewritten as

$$\mathbf{A}'(\omega) = \boldsymbol{\mathcal{T}}(\omega)\mathbf{A}(\omega). \tag{2.8}$$

If more samples and/or optical elements are included eq. (2.8) can be generalized to

$$\mathbf{A}'(\omega) = \boldsymbol{\mathcal{J}}_n \cdots \boldsymbol{\mathcal{T}}_n \cdots \boldsymbol{\mathcal{T}}_1(\omega) \cdots \boldsymbol{\mathcal{J}}_1\mathbf{A}(\omega). \tag{2.9}$$

Starting from eq. (2.7) $\boldsymbol{\mathcal{T}}(\omega)$ will be expressed in terms of the matix elements of the forward scattering amplitude $\boldsymbol{\mathcal{F}}(\omega)$. In the case of a scalar scattering amplitude the relation to the index of refraction $n(\omega)$ is for example given in [13]. Applying the same equation to matrices the relation between $\tilde{n}(\omega)$ and $\boldsymbol{\mathcal{F}}(\omega)$ is

$$\tilde{n}(\omega) = \sqrt{\tilde{\mathbf{1}} + 4\pi\lambda\!\!\!^{-2}\eta\boldsymbol{\mathcal{F}}(\omega)} \simeq \tilde{\mathbf{1}} + 2\pi\lambda\!\!\!^{-2}\eta\boldsymbol{\mathcal{F}}(\omega), \tag{2.10}$$

where $\tilde{\mathbf{1}}$ is the 2×2 unit matrix, $\lambda\!\!\!^{-} = \lambda/2\pi = 1/k_0 = c/\omega$ and η is the atomic volume density.[3] Expressing the forward scattering amplitude in the form of a 2×2 matrix in the Jones representation yields

$$\boldsymbol{\mathcal{F}}(\omega) = \begin{bmatrix} F_{\sigma\sigma}(\omega) & F_{\sigma\pi}(\omega) \\ F_{\pi\sigma}(\omega) & F_{\pi\pi}(\omega) \end{bmatrix}. \tag{2.11}$$

The subscripts ij refer to the polarization of the scattered (i) and incident (j) photon, respectively. Using the relation in eq. (2.10), eq. (2.7) can be rewritten as

$$\mathbf{A}'(\omega) = \mathrm{e}^{\mathrm{i}k_0 L}\mathrm{e}^{\mathrm{i}d\boldsymbol{\mathcal{F}}(\omega)}\mathbf{A}(\omega), \tag{2.12}$$

with $d = \lambda\eta L$. The first exponential in eq. (2.12) is a scalar and accounts for the phase shift of the unperturbed wave after traveling the distance L. To express the second exponential in eq. (2.12) in the form of a 2×2 matrix one can expand $\boldsymbol{\mathcal{F}}(\omega)$ in terms of Pauli matrices defined as

$$\widehat{\sigma} = (\sigma_x, \sigma_y, \sigma_z) = \left(\begin{bmatrix} 0 & 1 \\ 1 & 0 \end{bmatrix}, \begin{bmatrix} 0 & -\mathrm{i} \\ \mathrm{i} & 0 \end{bmatrix}, \begin{bmatrix} 1 & 0 \\ 0 & -1 \end{bmatrix} \right), \tag{2.13}$$

through

$$\boldsymbol{\mathcal{F}}(\omega) = a\tilde{\mathbf{1}} + \mathbf{b}\widehat{\sigma}, \tag{2.14}$$

where a and $\mathbf{b} = (b_x, b_y, b_z)$ are the expansion coefficients. It then follows directly that

$$\begin{aligned} a &= \frac{1}{2}\big(F_{\sigma\sigma}(\omega) + F_{\pi\pi}(\omega)\big), \\ b_x &= \frac{1}{2}\big(F_{\sigma\pi}(\omega) + F_{\pi\sigma}(\omega)\big), \\ b_y &= \frac{\mathrm{i}}{2}\big(F_{\sigma\pi}(\omega) - F_{\pi\sigma}(\omega)\big), \\ b_z &= \frac{1}{2}\big(F_{\sigma\sigma}(\omega) - F_{\pi\pi}(\omega)\big). \end{aligned} \tag{2.15}$$

Defining the unit vector $\hat{b} = \mathbf{b}/b$, with

$$b = \sqrt{b_x^2 + b_y^2 + b_z^2} = \sqrt{\frac{1}{4}\big[F_{\sigma\sigma}(\omega) - F_{\pi\pi}(\omega)\big]^2 + F_{\pi\sigma}(\omega)F_{\sigma\pi}(\omega)}, \tag{2.16}$$

[3] More generally, the term $\eta\boldsymbol{\mathcal{F}}(\omega)$ is written as $\sum_i \eta_i \boldsymbol{\mathcal{F}}_i(\omega)$, where i indicates the different atomic species. We will limit our discussion to a single atomic species, namely, that of Fe.

allows the use of the identity $(\hat{b}\cdot\widehat{\sigma})^2 = \tilde{\mathbf{1}}$, and after rearranging even and odd powers, the second exponential from eq. (2.12) can be written as

$$\mathrm{e}^{\mathrm{i}d\boldsymbol{\mathcal{F}}(\omega)} = \mathrm{e}^{\mathrm{i}da}\left[\tilde{\mathbf{1}}\cos(bd) + \mathrm{i}\left(\hat{b}\cdot\widehat{\sigma}\right)\sin(bd)\right]. \tag{2.17}$$

Consequently, $\boldsymbol{\mathcal{T}}(\omega)$ can be written as

$$\boldsymbol{\mathcal{T}}(\omega) = \mathrm{e}^{\mathrm{i}k_0 L}\,\mathrm{e}^{\mathrm{i}ad}\begin{bmatrix}\cos(bd) + \dfrac{\mathrm{i}}{b}b_z\sin(bd) & \dfrac{\mathrm{i}}{b}(b_x - \mathrm{i}b_y)\sin(bd)\\ \dfrac{\mathrm{i}}{b}(b_x + \mathrm{i}b_y)\sin(bd) & \cos(bd) - \dfrac{\mathrm{i}}{b}b_z\sin(bd)\end{bmatrix}. \tag{2.18}$$

Since the term $\exp(\mathrm{i}k_0 L)$ does not affect any of the results discussed further on, it will, therefore, be omitted, and the matrix elements of $\boldsymbol{\mathcal{T}}(\omega)$ written as

$$\begin{aligned}
T_{\sigma\sigma}(\omega) &= \mathrm{e}^{\mathrm{i}ad}\left[\cos(bd) + \frac{\mathrm{i}}{b}b_z\sin(bd)\right],\\
T_{\sigma\pi}(\omega) &= \mathrm{e}^{\mathrm{i}ad}\left[\frac{\mathrm{i}}{b}(b_x - \mathrm{i}b_y)\sin(bd)\right],\\
T_{\pi\sigma}(\omega) &= \mathrm{e}^{\mathrm{i}ad}\left[\frac{\mathrm{i}}{b}(b_x + \mathrm{i}b_y)\sin(bd)\right],\\
T_{\pi\pi}(\omega) &= \mathrm{e}^{\mathrm{i}ad}\left[\cos(bd) - \frac{\mathrm{i}}{b}b_z\sin(bd)\right].
\end{aligned} \tag{2.19}$$

Equation (2.18) is generally valid for $\boldsymbol{\mathcal{F}}(\omega)$ expressed in terms of a linear basis. It can therefore be applied to the transmission of radiation through any medium where the index of refraction $\tilde{n}(\omega)$ is given by eq. (2.10).

2.3. The forward scattering amplitude $\boldsymbol{\mathcal{F}}(\omega)$

Forward scattering of 14.4 keV X-rays from α-Fe containing ^{57}Fe nuclei contains two contributions, scattering from electrons and resonant scattering from ^{57}Fe nuclei. Over the frequency range where nuclear resonant scattering is significant, scattering from electrons is essentially constant and $\boldsymbol{\mathcal{F}}(\omega)$ can be written as

$$\boldsymbol{\mathcal{F}}(\omega) = \boldsymbol{\mathcal{F}}^{\mathrm{n}}(\omega) + \boldsymbol{\mathcal{F}}^{\mathrm{e}}, \tag{2.20}$$

where the indices n and e refer to "nuclear" and "electronic", respectively.

2.3.1. The nuclear forward scattering amplitude $\boldsymbol{\mathcal{F}}^{\mathrm{n}}(\omega)$

In the case of an unsplit resonance, the nuclear forward scattering amplitude $\boldsymbol{\mathcal{F}}^{\mathrm{n}}(\omega)$ has a scalar form given by [14]

$$F^{\mathrm{n}}(\omega) = \frac{1}{4}\lambda\!\!\!^{-}\, p f_{\mathrm{LM}}\left(\frac{1}{1+\alpha}\right)\left(\frac{2j_1+1}{2j_0+1}\right)\frac{\Gamma}{\hbar(\omega_0-\omega) - \mathrm{i}\Gamma/2}, \tag{2.21}$$

where f_{LM} is the Lamb–Mössbauer factor, p is the isotopic abundance of ^{57}Fe nuclei, α is the conversion coefficient, j_1 and j_0 are the spin quantum numbers of the excited

state and ground state, respectively, Γ is the natural linewidth, and ω_0 is the resonance frequency.[4] In this case the resonant scattering does not change the polarization of the scattered photon.

In the presence of hyperfine splittings $\boldsymbol{\mathcal{F}}^{\mathrm{n}}(\omega)$ becomes more complicated, since the resulting transitions have different polarization properties. Before the results are given in eqs. (2.24) and (2.25) the transition scheme of the 14.4 keV ^{57}Fe resonance is briefly discussed.

The ground state of ^{57}Fe has parity $p_0 = (-)$, a spin with quantum number $j_0 = 1/2$ and z-components $m_0 = \pm 1/2$. The 14.4 keV level has parity $p_1 = (-)$ and spin $j_1 = 3/2$ with z-components $m_1 = \pm 1/2, \pm 3/2$. If the hyperfine fields acting on the nucleus have a common axis, nuclear states involved in a γ-transition can be expressed in terms of eigenfunctions of angular momentum and parity, which are the quantities conserved in the γ-transition. The resulting radiation can be expressed as electric and magnetic 2^l-pole fields in terms of vector spherical harmonics. A multipole with order $l = 1$ is called dipole, one with $l = 2$ quadrupole and so on. From the transformation properties of the multipole fields under parity change it follows that electric multipole radiation has the parity $(-1)^l$, and magnetic multipole radiation has the parity $(-1)^{l+1}$. Conservation of parity therefore leads to the condition

$$\begin{aligned} p_0 &= (-1)^l p_1 \quad \text{for electric } 2^l \text{ radiation,} \\ p_0 &= (-1)^{l+1} p_1 \quad \text{for magnetic } 2^l \text{ radiation.} \end{aligned} \tag{2.22}$$

A 2^l-pole field corresponds to photons with spin l and z-component m. Conservation of angular momentum $\mathbf{j}_1 = \mathbf{j}_0 + \mathbf{l}$ leads to

$$|j_0 - j_1| \leqslant l \leqslant j_0 + j_1, \qquad m = m_1 - m_0, \tag{2.23}$$

and therefore, $l = 1, 2$ as possible spins for a photon in a $3/2 \rightarrow 1/2$ transition. This condition combined with the conservation of parity eq. (2.22) results in M1 (magnetic dipole) and E2 (electric quadrupole) for the allowed γ-transitions at the 14.4 keV ^{57}Fe resonance. Magnetic transitions are generally some orders of magnitude less probable than electric transitions of the same multipolarity. On the other hand, the transition probability is approximately proportional to $(2\pi R/\lambda)^{2l}$, where R is the radius of the nucleus.[5] For ^{57}Fe $(2\pi R/\lambda) \simeq 3 \cdot 10^{-4}$ at 14.4 keV and therefore the probability of a dipole transition is 10^9 times larger than that of a quadrupole transition. This factor overcomes the inherent weakness of the magnetic transitions, and consequently that the ^{57}Fe transition has essentially complete M1 character. This has been confirmed by measurements which show the fraction resulting from the E2 transition to be less than 10^{-4}. The resulting well-known M1-transition scheme for ^{57}Fe in α-Fe is shown in figure 3.

[4] F^{n} is (except for the factors p and f_{LM}) related to the total nuclear absorption cross-section σ_{n} through the optical theorem given by $\sigma_{\mathrm{n}} = (4\pi/k_0)\mathrm{Im}(F^{\mathrm{n}})$.

[5] This result assumes a central potential for the nucleus.

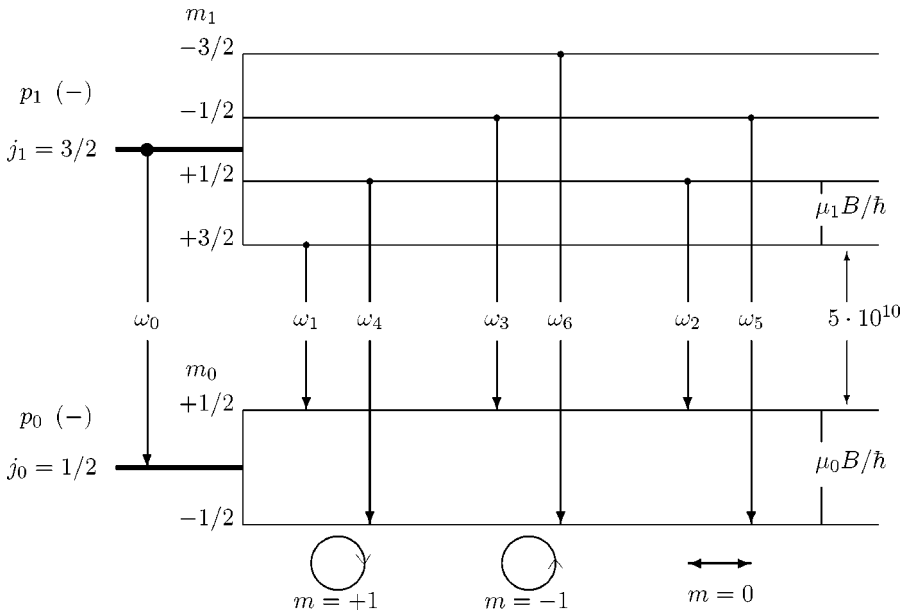

Figure 3. M1 transition scheme of ^{57}Fe in the presence of a magnetic field acting on the nucleus. The scale of ω_0 is reduced by a factor $5 \cdot 10^{10}$ compared to that of the splitting of the levels.

In α-Fe (since the cubic symmetry ensures that the electric field gradient is zero) the splitting is only determined by the nuclear Zeeman effect and, therefore, given by $\mu_i B$, where μ_i is the nuclear magnetic moment and B the magnitude of the **B**-field acting on the nucleus. The right and left circular polarizations shown in figure 3 correspond to photons emitted in the direction of the **B**-field at the nucleus. Photons resulting from a $\Delta m = 0$ transition are purely σ-polarized if they are emitted perpendicular to a vertical **B**-field.

Assuming a pure M1-transition and an equal population probability for both ground states one can show [15] that the matrix elements of the forward scattering amplitude $\mathcal{F}^{\mathrm{n}}(\omega)$ expressed in a linear basis are given by

$$
\begin{aligned}
F^{\mathrm{n}}_{\sigma\sigma}(\omega) &= \frac{3}{8}\lambda p\big[F_1 + F_{-1} + \big(\hat{\pi}\cdot\widehat{B}\big)^2(2F_0 - F_1 - F_{-1})\big],\\
F^{\mathrm{n}}_{\sigma\pi}(\omega) &= \frac{3}{8}\lambda p\big[-\mathrm{i}\big(\hat{k_0}\cdot\widehat{B}\big)(F_1 - F_{-1}) - \big(\hat{\sigma}\cdot\widehat{B}\big)\big(\hat{\pi}\cdot\widehat{B}\big)(2F_0 - F_1 - F_{-1})\big],\\
F^{\mathrm{n}}_{\pi\sigma}(\omega) &= \frac{3}{8}\lambda p\big[\mathrm{i}\big(\hat{k_0}\cdot\widehat{B}\big)(F_1 - F_{-1}) - \big(\hat{\sigma}\cdot\widehat{B}\big)\big(\hat{\pi}\cdot\widehat{B}\big)(2F_0 - F_1 - F_{-1})\big],\\
F^{\mathrm{n}}_{\pi\pi}(\omega) &= \frac{3}{8}\lambda p\big[F_1 + F_{-1} + \big(\hat{\sigma}\cdot\widehat{B}\big)^2(2F_0 - F_1 - F_{-1})\big],
\end{aligned}
\tag{2.24}
$$

where the γ-transition amplitudes F_m are defined as

$$
\begin{aligned}
F_0(\omega) &= f_{\mathrm{LM}}\left(\frac{1}{1+\alpha}\right)\left(\frac{1}{2j_0+1}\right)\Gamma \\
&\quad\times\left[\frac{C^2((1/2)\to(1/2))}{\hbar(\omega_2-\omega)-\mathrm{i}\Gamma/2}+\frac{C^2(-(1/2)\to-(1/2))}{\hbar(\omega_5-\omega)-\mathrm{i}\Gamma/2}\right], \\
F_1(\omega) &= f_{\mathrm{LM}}\left(\frac{1}{1+\alpha}\right)\left(\frac{1}{2j_0+1}\right)\Gamma \\
&\quad\times\left[\frac{C^2((3/2)\to(1/2))}{\hbar(\omega_1-\omega)-\mathrm{i}\Gamma/2}+\frac{C^2((1/2)\to-(1/2))}{\hbar(\omega_4-\omega)-\mathrm{i}\Gamma/2}\right], \\
F_{-1}(\omega) &= f_{\mathrm{LM}}\left(\frac{1}{1+\alpha}\right)\left(\frac{1}{2j_0+1}\right)\Gamma \\
&\quad\times\left[\frac{C^2(-(1/2)\to(1/2))}{\hbar(\omega_3-\omega)-\mathrm{i}\Gamma/2}+\frac{C^2(-(3/2)\to-(1/2))}{\hbar(\omega_6-\omega)-\mathrm{i}\Gamma/2}\right].
\end{aligned}
\tag{2.25}
$$

$C(m_1\to m_0)$ are the Clebsch–Gordan coefficients resulting from the summation rules of angular momentum in a $\frac{3}{2}\to\frac{1}{2}$ dipole transition and are given by

$$
\begin{aligned}
C\left(\frac{3}{2}\to\frac{1}{2}\right) &= C\left(-\frac{3}{2}\to-\frac{1}{2}\right)=1, \\
C\left(\frac{1}{2}\to\frac{1}{2}\right) &= C\left(-\frac{1}{2}\to-\frac{1}{2}\right)=\sqrt{\frac{2}{3}}, \\
C\left(\frac{1}{2}\to-\frac{1}{2}\right) &= C\left(-\frac{1}{2}\to\frac{1}{2}\right)=\sqrt{\frac{1}{3}},
\end{aligned}
\tag{2.26}
$$

and the frequencies ω_i are shown in figure 3. Furthermore, the vectors $\hat{\sigma}, \hat{\pi}$ and $\hat{k}_0$ are the unit vectors which form the basis in which the direction of the quantization axis $\widehat{B}$

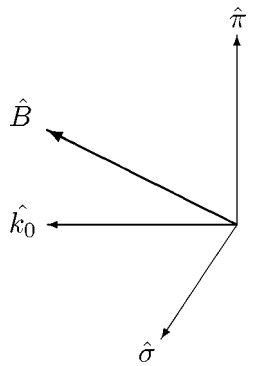

Figure 4. Quantization axis $\widehat{B}$ in the linear basis.

Table 2
Parameters of the 14.4 keV ^{57}Fe level in metallic Fe. The last three parameters are room temperature values.

Parameters of the 14.4 keV ^{57}Fe resonance	
$\hbar\omega_0$	14.41303 ± 0.00008 keV
Γ	4.665 ± 0.007 neV
τ_0	141.11 ± 0.2 ns
α	8.21 ± 0.12
f_{LM}	0.771 ± 0.017
$\mu_0 B$	188.25 ± 0.08 neV
$\mu_1 B$	-107.51 ± 0.04 neV

is expressed. The letter B is chosen to indicate that the quantization axis for ^{57}Fe in a metallic environment is only determined by the **B**-field acting on the nucleus. Figure 4 shows the geometry.

The parameters for the 14.4 keV level of ^{57}Fe are summarized in table 2. The values are from [16] except for f_{LM}, which is from [17].

2.3.2. Some polarization properties of $\boldsymbol{\mathcal{F}}^{\mathrm{n}}(\omega)$

As mentioned in the definition of $\boldsymbol{\mathcal{F}}^{\mathrm{n}}(\omega)$ a matrix element F^{n}_{ij} corresponds to the amplitude of a photon with polarization j being forward scattered with its polarization resulting in i. Since eqs. (2.24) and (2.25) are somewhat complicated, three simple geometries will now be discussed to illustrate how forward scattering from ^{57}Fe affects the polarization:

1. The single line case occurs when the magnitude of the **B**-field is zero. In this case $\omega_i = \omega_0$ for all six lines and consequently $F_0 = F_1 = F_{-1}$. $\boldsymbol{\mathcal{F}}^{\mathrm{n}}(\omega)$ then results in

$$\boldsymbol{\mathcal{F}}^{\mathrm{n}} = \begin{bmatrix} 1 & 0 \\ 0 & 1 \end{bmatrix} F^{\mathrm{n}}, \tag{2.27}$$

   where F^{n} is given in eq. (2.21), showing that the polarization of a scattered photon is not affected.

2. Consider that the **B**-field at the nucleus is parallel to $\hat{\pi}$. In this case $(\hat{\pi} \cdot \widehat{B}) = 1$, $(\widehat{\sigma} \cdot \widehat{B}) = (\hat{k}_0 \cdot \widehat{B}) = 0$, and $\boldsymbol{\mathcal{F}}^{\mathrm{n}}(\omega)$ is simply given by

$$\boldsymbol{\mathcal{F}}^{\mathrm{n}} = \mathrm{const} \begin{bmatrix} F_0 & 0 \\ 0 & F_1 + F_{-1} \end{bmatrix}, \tag{2.28}$$

   showing that forward scattering does not change the polarization of a pure σ- or π-polarized incident photon. It, furthermore, shows that an incident σ-polarized photon ($[1, 0]$) only couples to F_0 and an incident π-polarized photon ($[0, 1]$) only couples to $F_{\pm 1}$.
   It is helpful to study some selected frequencies. Consider the case when the splittings $\hbar\delta\omega_i = \hbar(\omega_0 - \omega_i)$ are large compared to Γ. Then, at any frequency at most

one of the six Lorentzians in eq. (2.25) differs significantly from zero. If the frequency of the incident photon is either $\omega = \omega_2$ or ω_5, the scattering amplitude can be approximated by

$$\mathcal{F}^{\mathrm{n}} \simeq \text{const} \begin{bmatrix} 1 & 0 \\ 0 & 0 \end{bmatrix}. \tag{2.29}$$

Consequently, at the resonance frequencies of the $\Delta m = 0$ transitions the ^{57}Fe nucleus acts like a linear horizontal polarizer. Similarly, at $\omega = \omega_1, \omega_3, \omega_4, \omega_6$

$$\mathcal{F}^{\mathrm{n}} \simeq \text{const} \begin{bmatrix} 0 & 0 \\ 0 & 1 \end{bmatrix}, \tag{2.30}$$

corresponding to a linear vertical polarizer.

3. Another simple geometry is given by $\widehat{B} \parallel \hat{k}_0$. In this case $(\hat{k}_0 \cdot \widehat{B}) = 1$, $(\widehat{\sigma} \cdot \widehat{B}) = (\hat{\pi} \cdot \widehat{B}) = 0$, and $\mathcal{F}^{\mathrm{n}}(\omega)$ results in

$$\mathcal{F}^{\mathrm{n}} = \text{const} \begin{bmatrix} F_1 + F_{-1} & -\mathrm{i}(F_1 - F_{-1}) \\ \mathrm{i}(F_1 - F_{-1}) & F_1 + F_{-1} \end{bmatrix}. \tag{2.31}$$

Again, it is helpful to select some resonance frequencies. At $\omega = \omega_1, \omega_4$, the resonance frequencies for the $\Delta m = +1$ transitions $\mathcal{F}^{\mathrm{n}}(\omega)$ can be approximated by

$$\mathcal{F}^{\mathrm{n}} \simeq \text{const} \begin{bmatrix} 1 & -\mathrm{i} \\ \mathrm{i} & 1 \end{bmatrix}, \tag{2.32}$$

which is the Jones matrix of a right circular polarizer. Similarly, $\mathcal{F}^{\mathrm{n}}(\omega)$ results in the Jones matrix for a left circular polarizer at frequencies $\omega = \omega_3, \omega_6$, which correspond to a $\Delta m = -1$ transition. If $\widehat{B}$ is antiparallel to $\hat{k}_0$, the polarizations are reversed.

In general, at a given frequency and scattering geometry, $\mathcal{F}^{\mathrm{n}}(\omega)$ can be expressed as a Jones matrix, showing that the ^{57}Fe nucleus acts like a linear, elliptical or circular polarizer for resonantly forward scattered photons. Since an incident SR pulse contains a wide range of frequency components that cover all resonances, the optical effects arising from the transmission of such a pulse through a scattering medium described by $\mathcal{F}^{\mathrm{n}}(\omega)$ can result in a complex mixture of different polarizations. Some of the resulting polarization effects are calculated and discussed later in this section, together with experimental results.

2.3.3. The electronic forward scattering amplitude $\mathcal{F}^{\mathrm{e}}$

Electronic forward scattering of 14.4 keV X-rays in metallic Fe does not show significant anomalous polarization effects (no absorption edge is in the vicin-

ity of 14.4 keV). $\mathcal{F}^{\mathrm{e}}$ is, therefore, to a good approximation, diagonal and given by

$$\mathcal{F}^{\mathrm{e}} \simeq -\begin{bmatrix} 1 & 0 \\ 0 & 1 \end{bmatrix}\left(Zr_{\mathrm{e}} - \mathrm{i}\frac{\sigma_{\mathrm{e}}}{4\pi\lambda}\right), \tag{2.33}$$

where Z is the atomic number of Fe, r_{e} the classical electron radius, and σ_{e} is the total electronic absorption cross-section with contributions of photoelectric absorption and Compton scattering. For the calculation of the transmission amplitude $\mathcal{T}(\omega)$ it is sufficient to include the imaginary part of $\mathcal{F}^{\mathrm{e}}$ since the real part only contributes a phase shift. The result is a reduction of $\mathcal{T}(\omega)$ by a factor $\exp(-(1/2)\mu_{\mathrm{e}}L)$, where $\mu_{\mathrm{e}} = \eta\sigma_{\mathrm{e}}$ is the electronic absorption factor. (At 14.4 keV $\mu_{\mathrm{e}} \simeq 500$ cm^{-1}.)

2.3.4. Summary of the calculation of $\mathcal{T}(\omega)$

Thus, the transmission matrix $\mathcal{T}(\omega)$ is now fully determined. The important steps and equations which lead to $\mathcal{T}(\omega)$ are summarized as follows:

1. Determine the Mössbauer parameters. (For room temperature they are given in table 2.)

2. Calculate the transition amplitudes F_m given in eq. (2.25) for the appropriate splittings.

3. Determine the orientation of the **B**-field (see figure 4) and relate it to the dot products in eq. (2.24).

4. Calculate the matrix elements of $\mathcal{F}(\omega)$ (eq. (2.20)) with $\mathcal{F}^{\mathrm{n}}(\omega)$ (eq. (2.24)) and $\mathcal{F}^{\mathrm{e}}$ (eq. (2.33)).

5. Relate $\mathcal{F}(\omega)$ to $\mathcal{T}(\omega)$ with the use of eqs. (2.11), (2.15), (2.16) and (2.19).

2.4. The relation of $\mathcal{T}(\omega)$ to the intensity $I(t)$

The description of the resonant medium in terms of a transmission matrix $\mathcal{T}(\omega)$ does not include the amplitude of the incident electromagnetic wave $\mathbf{A}(\omega)$. To calculate the time dependent intensity $I(t)$, the amplitude $\mathbf{A}'(\omega)$ and therefore $\mathbf{A}(\omega)$ has to be known (see eq. (2.8)). A simple relation between $\mathbf{A}'(\omega)$ and $\mathcal{T}(\omega)$ exists only if $\mathbf{A}(\omega)$ is constant over the frequency range where $\mathcal{T}(\omega)$ is frequency dependent. This requirement is fulfilled if the frequency spectrum of $\mathbf{A}(\omega)$ ranges from frequencies somewhat smaller than ω_1 to frequencies somewhat larger than ω_6. Since even for low temperatures, where the magnetic splitting is largest, this frequency range corresponds to less than 10^{-10} of the resonance energy, any quasimonochromatic incident wave other than Mössbauer radiation fulfills this requirement. If, furthermore, the incident wave is polarized, $\mathbf{A}(\omega)$ can be epressed as a Jones vector. Then the intensity as a

function of time $I(t)$ is given by the modulus square of the inverse Fourier transform of $\mathbf{A}'(\omega)$, i.e.,

$$I(t) = \left|\mathbf{A}'(t)\right|^2 = \left|\mathrm{FT}^{-1}\left(\mathbf{A}'(\omega)\right)\right|^2 = \left|\frac{1}{2\pi}\int_0^\infty \mathbf{A}'(\omega)\mathrm{e}^{-\mathrm{i}\omega t}\,\mathrm{d}\omega\right|^2, \tag{2.34}$$

and is directly related to the matrix elements of $\boldsymbol{\mathcal{T}}(\omega)$.[6]

The two geometries corresponding to the experiments performed are now calculated. If a horizontal linear polarizer is applied, $\mathbf{A}'(\omega)$ is given by

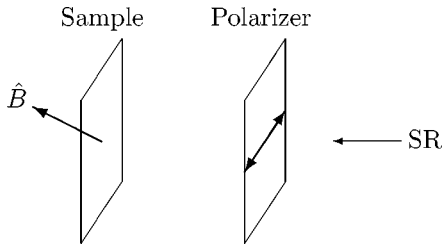

$$\mathbf{A}'(\omega) = A_\sigma \begin{bmatrix} T_{\sigma\sigma}(\omega) \\ T_{\pi\sigma}(\omega) \end{bmatrix} = \begin{bmatrix} T_{\sigma\sigma}(\omega) & T_{\sigma\pi}(\omega) \\ T_{\pi\sigma}(\omega) & T_{\pi\pi}(\omega) \end{bmatrix} \begin{bmatrix} 1 & 0 \\ 0 & 0 \end{bmatrix} \begin{bmatrix} A_\sigma \\ A_\pi \end{bmatrix}. \tag{2.35}$$

In practice the incident SR pulse is essentially σ-polarized $[A_\sigma, A_\pi] \simeq [1, 0]$ and the horizontal polarizer has only a small effect. The resulting intensity $I(t)$ is then given by

$$I(t) = I_{\sigma\sigma}(t) + I_{\pi\sigma}(t) = \left(\left|\mathrm{FT}^{-1}\left(T_{\sigma\sigma}(\omega)\right)\right|^2 + \left|\mathrm{FT}^{-1}\left(T_{\pi\sigma}(\omega)\right)\right|^2\right). \tag{2.36}$$

Including a vertical polarizer results in

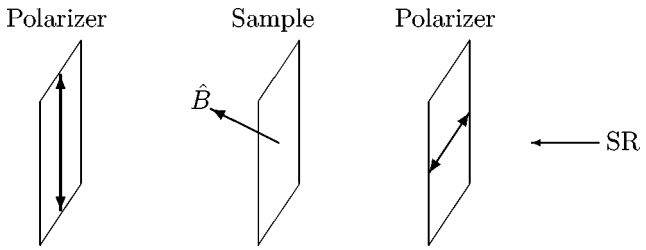

$$\mathbf{A}'(\omega) = \begin{bmatrix} 0 \\ T_{\pi\sigma}(\omega) \end{bmatrix} = \begin{bmatrix} 0 & 0 \\ 0 & 1 \end{bmatrix} \begin{bmatrix} T_{\sigma\sigma}(\omega) & T_{\sigma\pi}(\omega) \\ T_{\pi\sigma}(\omega) & T_{\pi\pi}(\omega) \end{bmatrix} \begin{bmatrix} 1 & 0 \\ 0 & 0 \end{bmatrix} \begin{bmatrix} A_\sigma \\ A_\pi \end{bmatrix}, \tag{2.37}$$

[6] Expressing $\mathbf{A}(\omega)$ as a Jones vector omits the proportionality factor $|A|^2$. For the following discussion this factor is not important. It is, however, important if one wants to calculate the counting rate for a given incident flux.

and therefore,

$$I(t) = I_{\pi\sigma}(t) = \left|\mathrm{FT}^{-1} T_{\pi\sigma}(\omega)\right|^2. \tag{2.38}$$

This geometry is suitable for investigating the effects of polarization mixing, since it isolates the matrix element corresponding to ($\sigma \rightarrow \pi$) scattering.

For SR-based experiments, an important aspect is the difficulty in measuring the delayed resonant scattering in the presence of extremely intense, but prompt, non-resonant scattering. This undesirable signal is a consequence of the relatively broad-band nature of even the highest-resolution crystal X-ray monochromators. Essentially all of the output from such a monochromator contributes to this prompt burst, whereas only a band of order 10^{-9} eV contributes to the resonant signal. It is fortunate that essentially all of this non-resonant scattering is ($\sigma \rightarrow \sigma$) scattering, and hence, is completely suppressed by a polarizer which only accepts π-polarized radiation. This idea has been tested with the newest synchrotron sources and has been shown to be extremely effective [8–10,18].

3. NFS for different geometries

To illustrate the phenomena related to NFS of polarized radiation, some special cases are calculated and discussed, using the formalism derived in the previous section. The polarization properties of $\boldsymbol{\mathcal{T}}(\omega)$ are similar to those of $\boldsymbol{\mathcal{F}}^{\mathrm{n}}(\omega)$. In addition, there are collective effects resulting from the fact that $\boldsymbol{\mathcal{T}}(\omega)$ represents a medium containing an ensemble of scatterers. Both are best shown by calculating $\mathbf{A}'(t)$ and $I(t)$.

3.1. No hyperfine splittings

First we consider the simplest case, in which no hyperfine field is acting on the nucleus and consequently $\delta\omega_i = 0$ for all i. In this single line case $\boldsymbol{\mathcal{F}}^{\mathrm{n}}(\omega)$ is given by eqs. (2.21) and (2.27). Consequently the transmission matrix $\boldsymbol{\mathcal{T}}(\omega)$ is given by

$$\mathcal{T}(\omega) = \mathrm{e}^{-\mu_{\mathrm{e}} L/2} \begin{bmatrix} 1 & 0 \\ 0 & 1 \end{bmatrix} \mathrm{e}^{\mathrm{i}\Gamma_c (1/(\hbar(\omega_0 - \omega) - \mathrm{i}\Gamma/2))}, \tag{3.1}$$

where the quantity Γ_c is called the enhanced decay width given by

$$\Gamma_c = \pi \lambda\!\!\!^{-2} p \eta L f_{\mathrm{LM}} \left(\frac{1}{1+\alpha}\right) \left(\frac{2j_1 + 1}{2(2j_0 + 1)}\right) \Gamma. \tag{3.2}$$

Consequently, $\mathbf{A}'(\omega)$ can be written as a scalar given by

$$A'(\omega) = \mathrm{e}^{-\mu_{\mathrm{e}} L/2} \mathrm{e}^{\mathrm{i}\Gamma_c [1/(\hbar(\omega_0 - \omega) - \mathrm{i}\Gamma/2)]} = \mathrm{e}^{-\mu_{\mathrm{e}} L/2} \mathrm{e}^{\mathrm{i}2\chi (1/(\Delta_0 - \mathrm{i}))}, \tag{3.3}$$

where $\chi = (\Gamma_c/\Gamma)$ is the effective thickness and $\Delta_0 = (2\hbar/\Gamma)(\omega_0 - \omega)$. Equation (3.1) shows that the scattered radiation does not change its state of polarization

and, hence, there are no phenomena of special interest to our primary discussion. However, it is important to understand the influence of the various factors on the scattering in this simple case if we are to follow the more complex scenarios in what follows.

For $A'(\omega)$ in eq. (3.1), the Fourier integral in eq. (2.35) yields a relatively simple solution (see, e.g., [19]), and in addition to a δ-function at $t = 0$ the resulting intensity $I(t)$ is given by

$$I(t) = \mathrm{e}^{-\mu_\mathrm{e} L} \mathrm{e}^{-t/\tau_0} \frac{\chi}{\tau_0 t} \mathrm{J}_1^2 \left[\sqrt{\frac{4\chi t}{\tau_0}} \right], \tag{3.4}$$

where J_1 is the first-order Bessel function. The result shows that $I(t)$ is not just an exponential, $\exp(-t/\tau_0)$, as would be expected for the decay of an isolated atom, but depends on χ. Figure 5 shows the real and imaginary parts of $A'(\omega)$ (where the exponential $\exp(-\mu_\mathrm{e} L/2)$ has been removed) and the corresponding $I(t)$ [7] for different values of χ. As can be seen in the figure, for $\chi = 1$, $\mathrm{Re}(A'(\omega))$ has approximately a Lorentzian form, and correspondingly $I(t)$ has an exponential form in the time window shown. Approximating eq. (3.4) with

$$I(t) \propto \chi^2 \mathrm{e}^{-(1+\chi)t/\tau_0}, \tag{3.5}$$

which is valid for $t < \tau_0/(1 + \chi)$, shows that generally the initial decay rate is exponential and enhanced by a factor $\exp(-\chi t/\tau_0)$. This indicates that in the limit of very small χ the decay time is that of an isolated atom. On the other hand, as χ increases, frequency components further away from ω_0 contribute to the resonant forward scattering. $A'(\omega)$ is no longer Lorentzian-like and, consequently, $I(t)$ has a non-exponential form with minima imposed by the Bessel function (dynamical beats). The fact that with increasing χ, frequency components further away from resonance contribute to the resonant scattering is similar to the well known thickness broadening in a conventional Mössbauer absorption spectrum. There is, however, an important difference due to the source. In contrast to the uniform spectrum provided by the SR pulse ($\mathbf{A}(\omega) = \mathrm{const}$), the spectrum provided by a conventional ^{57}Co source has an amplitude given by

$$A(\omega) \propto \frac{\Gamma}{\hbar(\omega_0 - \omega) - (\mathrm{i}\Gamma/2)}.$$

Therefore, $A'(\omega)$ and consequently $I(t)$ is different.[8] Only by using a short SR pulse is it possible to create a state whose decay is described by eq. (3.4) [20,21].

The easiest experimental way to change χ is by varying the sample thickness L. This experiment was one of the first NFS experiments to be performed, and clearly demonstrated the coherent nature of the forward scattering. Figures 6 and 7 show experimental data and calculations showing the speedup for thin samples, and the

[7] As for all the following time spectra, the intensity is normalized.

[8] In 1960 Lynch, Holland and Hammermesh measured the time dependence of forward scattering using a ^{57}Co source [22]. The corresponding $I(t)$ is given in their eq. (7) in which $\beta = 4\chi$.

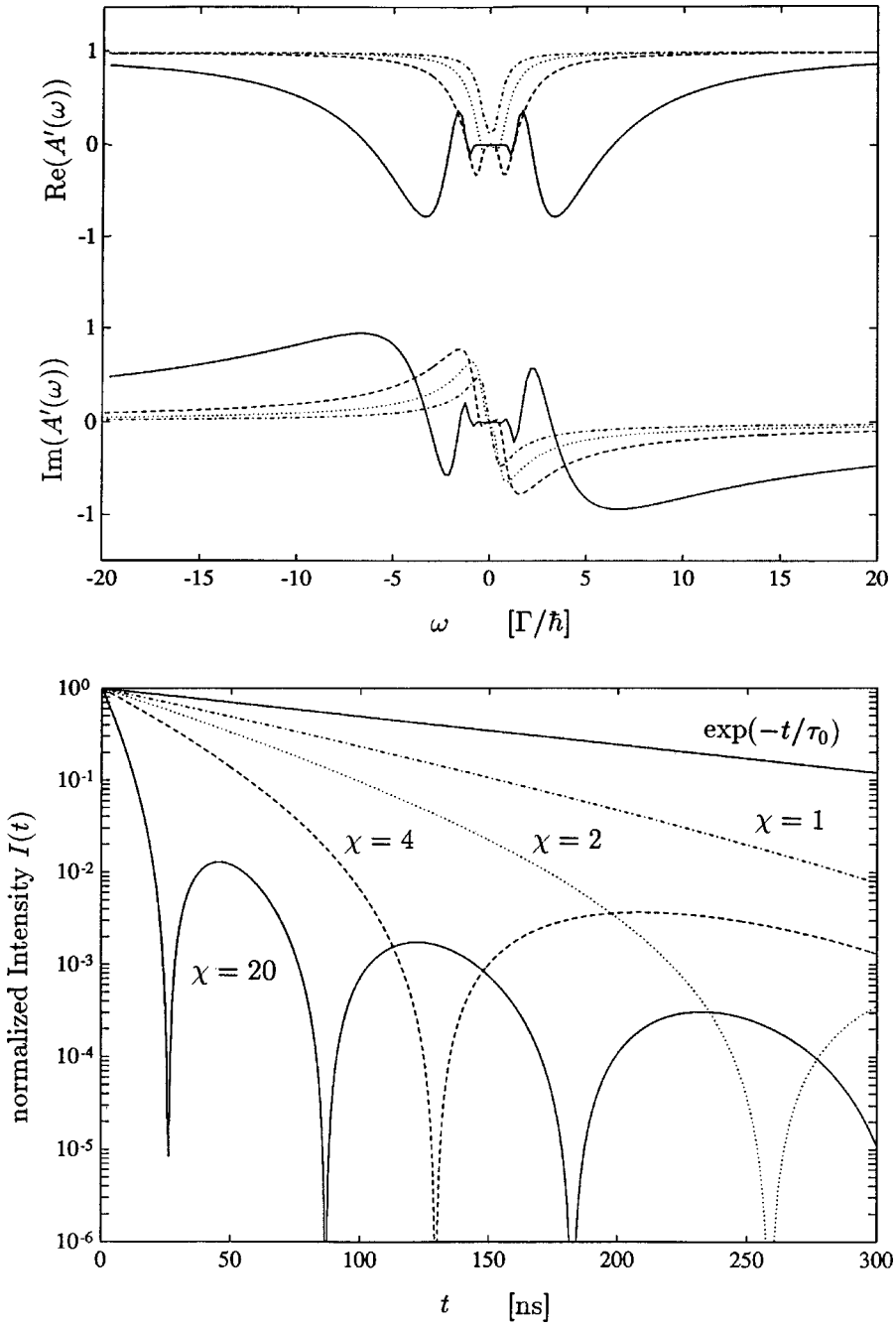

Figure 5. The top figure shows the real and imaginary parts of $A'(\omega)$ for a single line resonance with $\chi = 1$ (dot dashed line), $\chi = 2$ (dotted line), $\chi = 4$ (dashed line) and $\chi = 20$ (solid line). The bottom figure shows the corresponding intensities $I(t)$. The exponential function $\exp(-t/\tau_0)$ (top solid line) is shown for comparison.

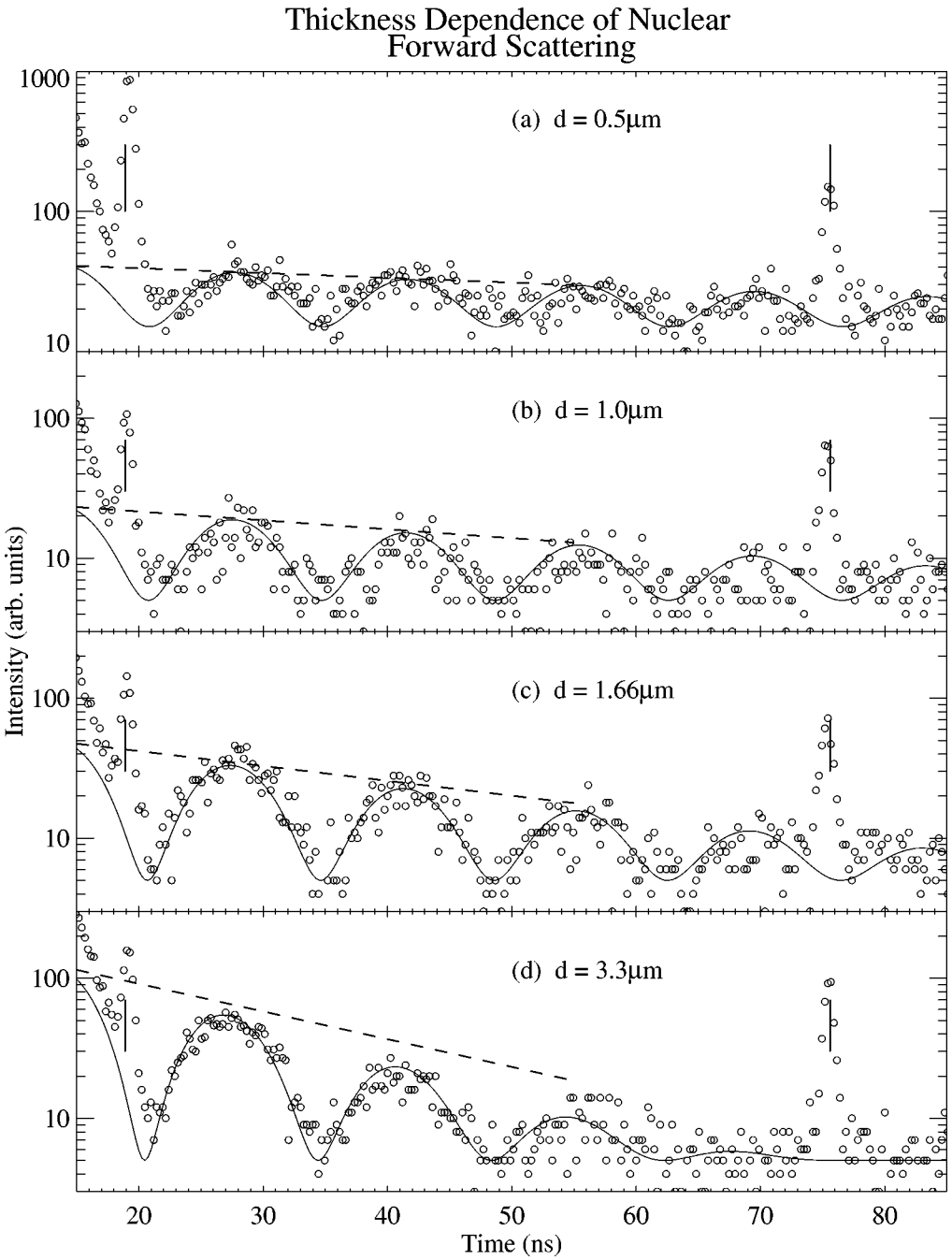

Figure 6. Time spectra of the NFS from thin polycrystalline $\mathcal{F}^e$ foils of different thicknesses. The dashed lines indicate the approximately exponential decay as calculated using eq. (3.5), while the solid lines are calculations using eq. (3.4). The vertical bars indicate the location of spurious electron bunches in the storage ring, and are irrelevant to the experiment.

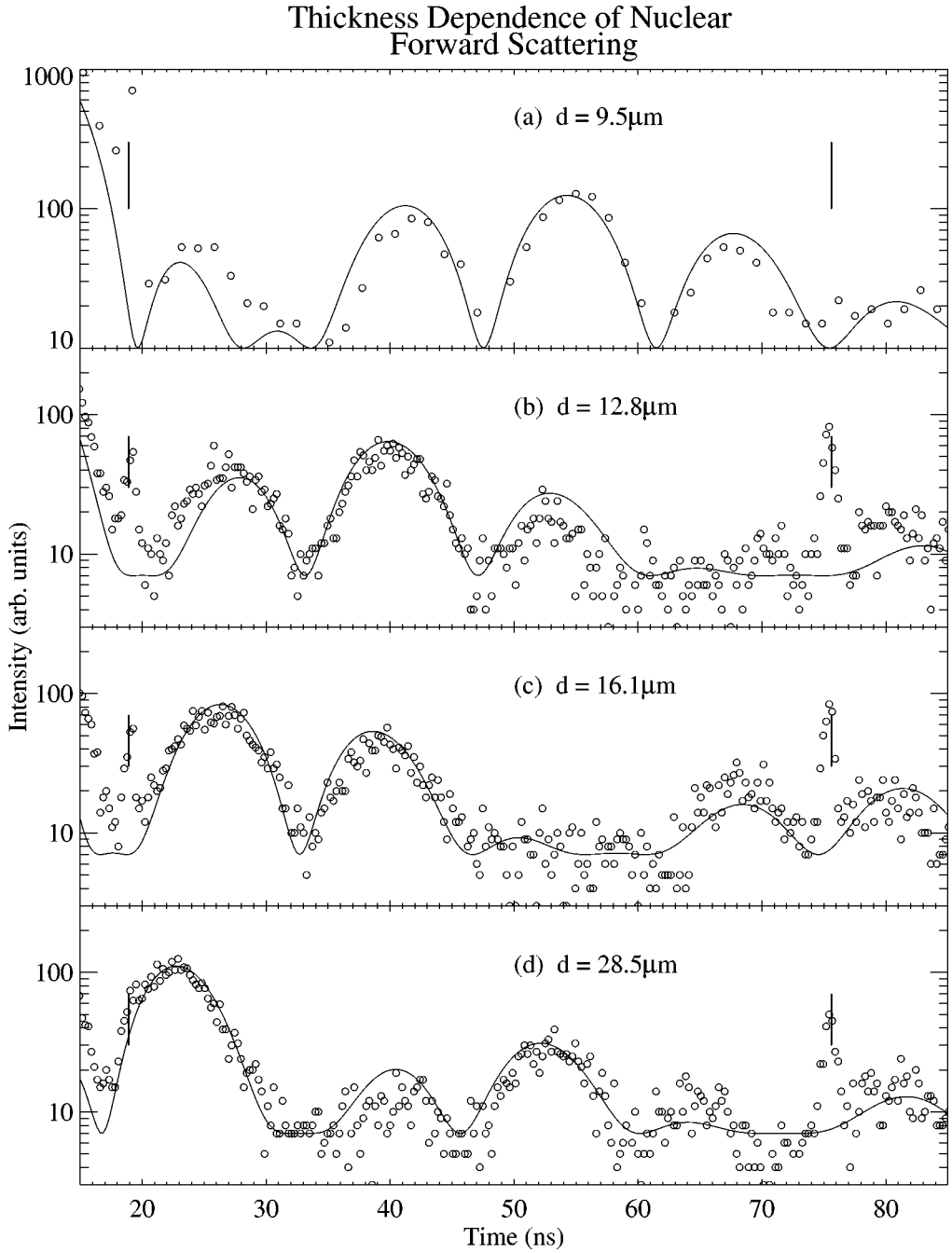

Figure 7. Time spectra of the NFS from thick polycrystalline $\mathcal{F}^e$ foils of different thicknesses. The solid lines are calculations using eq. (3.4).

transition from the approximation of eq. (3.5) to the strongly non-exponential behavior described by eq. (3.4).

3.2. σ-polarized beam and $\widehat{B} \parallel \hat{\pi}$

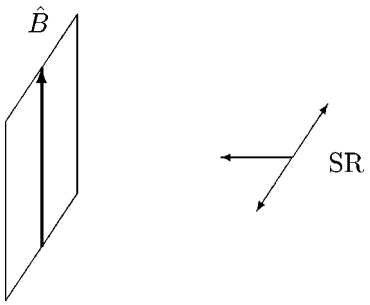

At temperatures below the Curie temperature an internal **B**-field acts on the ^{57}Fe nuclei embedded in metallic Fe. This leads to a splitting of the nuclear levels, as shown in figure 3. The internal field can be aligned through an applied external field resulting in a well defined orientation of $\widehat{B}$. In the following geometries a σ-polarized incident beam is assumed, since this corresponds to the experimental conditions for all the experiments we describe. The situation $\widehat{B} \parallel \hat{\pi}$, as shown above, results in

$$\left(\hat{\pi} \cdot \widehat{B}\right) = 1, \qquad \left(\hat{\sigma} \cdot \widehat{B}\right) = 0 \quad \text{and} \quad \left(\hat{k}_0 \cdot \widehat{B}\right) = 0,$$

and, as seen in eq. (2.28), $\boldsymbol{\mathcal{F}}^{\mathrm{n}}(\omega)$ is diagonal. As a consequence, $\boldsymbol{\mathcal{T}}(\omega)$ becomes diagonal, and for an incident σ-polarized beam eq. (2.35) applies, showing that $\mathbf{A}'(\omega)$ is just proportional to $T_{\sigma\sigma}(\omega)$, which now only depends on F_0. Performing the algebra results in

$$\mathbf{A}'(\omega) = \mathrm{e}^{-\mu_{\mathrm{e}} L/2} \begin{bmatrix} 1 \\ 0 \end{bmatrix} \mathrm{e}^{(3/2)\mathrm{i}\chi(2/(3(\Delta_2 - \mathrm{i})) + 2/(3(\Delta_5 - \mathrm{i}))}, \tag{3.6}$$

showing that only the two $\Delta m = 0$ lines contribute to the transmitted amplitude. The Fourier transform results in a more complicated form and is calculated numerically using a Fast Fourier Transform algorithm. If the two lines are well separated ($\hbar\delta\omega_{5,2} = \hbar(\omega_5 - \omega_2) > \Gamma_c$), a rather simple approximation for $I(t)$ is given by replacing χ with $\chi/2$ and multiplying eq. (3.4) with a cos^2-term. Figure 8 shows $I(t)$ for $\chi = 1$ and different splittings. The characteristic quantum beating of the two hyperfine-split lines can be seen in the spectra. For splittings larger than Γ_c, the two lines are well separated and the beat period is given by $T = 2\pi/\delta\omega_{5,2}$. The results shown in figures 6 and 7 are obtained in this geometry, and clearly show the simple two-line sinusoidal beating for small thicknesses. In this case there is also no mixing of polarization states, only a selective excitation of two of the possible transitions by virtue of the polarization of the incident beam.

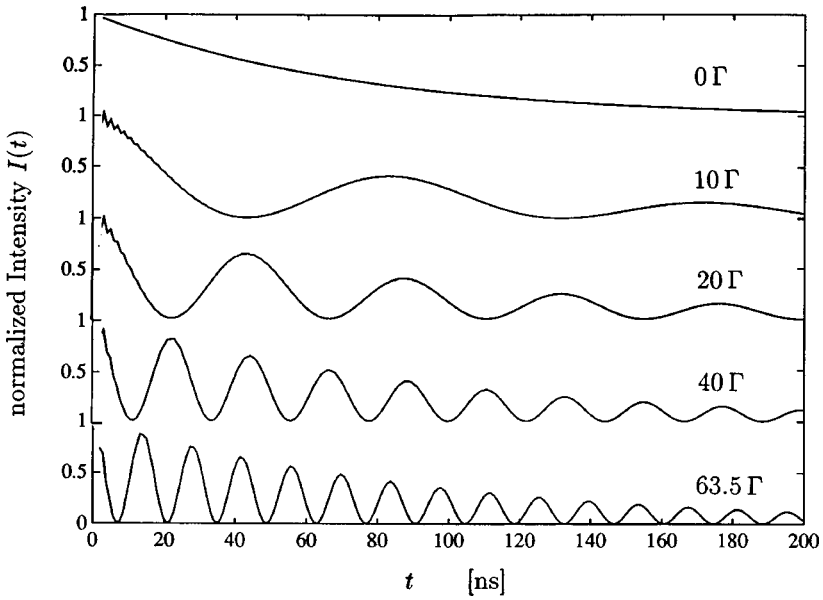

Figure 8. Comparison of time spectra in the geometry $\widehat{B} \parallel \hat{\pi}$ for $\chi = 1$ and splittings $\hbar(\omega_5 - \omega_2) = 0, 10, 20, 40, 63.5\,\Gamma$ (the last value indicates the splitting at room temperature).

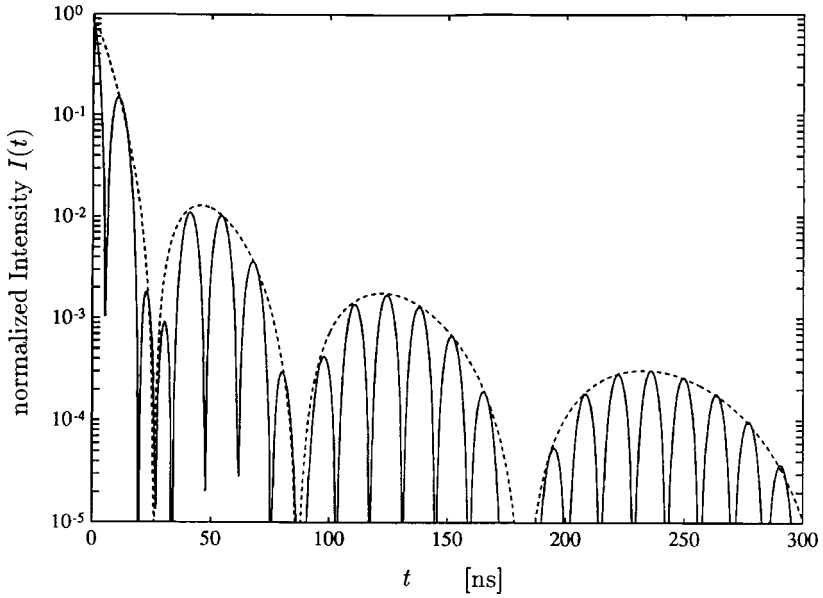

Figure 9. Comparison of a time spectrum in the geometry $\widehat{B} \parallel \hat{\pi}$ for $\chi = 40$ and $\hbar(\omega_5 - \omega_2) = 63.5\,\Gamma$, with a single line spectrum (dashed line) with $\chi = 20$.

At $\delta\omega_{5,2} = 0$ the lines collapse into a single line, and $I(t)$ is given by eq. (3.4), since adding the two exponents in eq. (3.6) leads to a single exponential as given in eq. (3.1). If χ is large, an additional modulation is superimposed on the quantum beats. This can be seen in figure 9, where $I(t)$ for $\chi = 40$ is compared with $I(t)$ for a single line with $\chi = 20$. As can be seen in figure 9, the single line spectrum corresponds to the envelope of a spectrum of well separated lines with twice the effective thickness χ. This indicates that in the $\Delta m = 0$ case the two transitions each have half the strength of the collapsed single line (see eq. (3.6)). This phenomenon can be observed by heating the NFS sample above the Curie temperature, which results in a collapse of the lines and at the same time a reduction in χ. Since changing the temperature results in a change of f_{LM} which, from eq. (3.2), directly affects χ, a measurement of $I(t)$ as a function of temperature is a direct way to determine the temperature dependence of f_{LM}, as was shown by Bergmann et al. [17]. Figure 10 shows a sequence of time spectra from that paper taken as a function of temperature. One can see both the effects of changes in the internal field, causing a reduction of the splitting and hence resulting in a reduction of the beat frequency, and changes in χ causing the envelope of the modulation to also become more slowly varying. At some point these three effects begin to compete; the collapsing of the lines causing an increase in χ, the decrease in f_{LM} causing a reduction in χ, and the changing beat pattern due to the decreased splitting. Indeed, as the internal field aproaches zero (at the Curie temperature), it becomes difficult to follow the details of quantum beats and Bessel-function behavior. As discussed previously, the Bessel behavior becomes even more pronounced as the split lines collapse onto each other, because the effective χ is doubled. The data contain enough information to allow all of these phenomena to be unscrambled and excellent determinations of f_{LM} to be extracted.

The interference of the ($\Delta m = 0$) transitions demonstrates spatial coherence between different ^{57}Fe nuclei, since the two ($\Delta m = 0$) transitions lead to different ground states.

NFS in the two-line case represents an interesting analogy to Young's double slit interference experiment. The quantum beats reflect the frequency difference of the lines, and the envelope reflects the line width (see top of figure 5). Similarly, in the double slit experiment the beating reflects the difference in position of the two slits and the envelope the slit width. In addition, the coherent illumination of the two slits necessary for the beats in the double slit experiment is analogous to the coherent excitation of the two ($\Delta m = 0$) levels provided by the SR source. However, a complete analogy fails, mainly due to causality. Since the real and imaginary parts of $\tilde{n}(\omega)$ are connected by the Kramers–Kronig relations, the real and imaginary parts of $A'(\omega)$ are such that $I(t)$ is zero at $t \leqslant 0$. Such a limitation does not exist in space, so that the intensity occurs both at positive and negative angles.

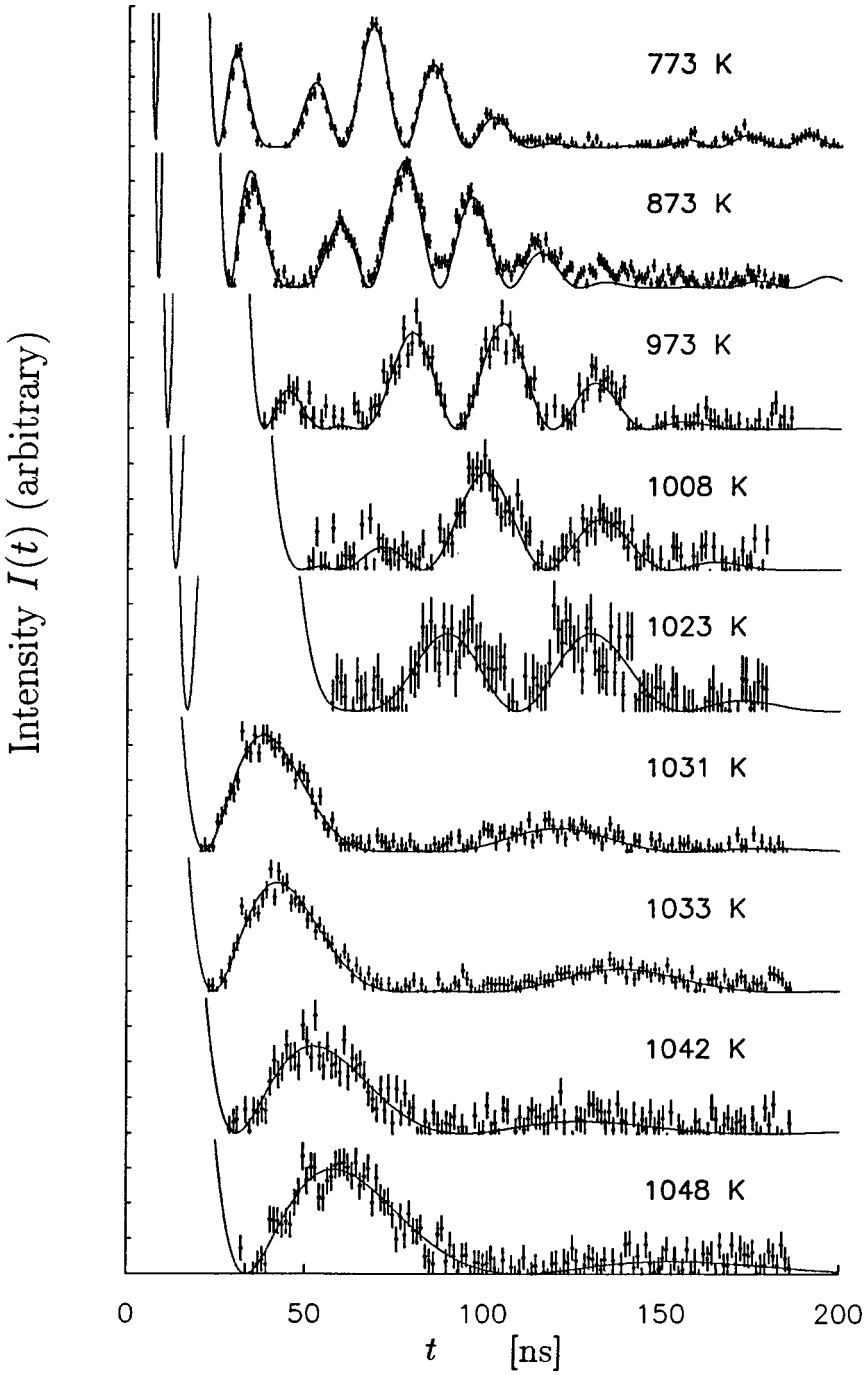

Figure 10. Time-dependent scattering as a function of temperature. The changes reflect the reduction in splitting as the internal field collapses and also the changing Lamb–Mössbauer factor as the temperature increases.

3.3. σ-polarized beam and $\widehat{B} \parallel \widehat{\sigma}$

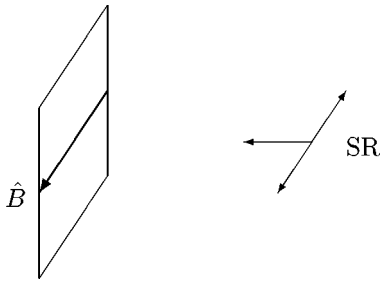

If the internal B-field is aligned parallel to the σ-direction as shown in the figure, the dot products result in $(\widehat{\sigma} \cdot \widehat{B}) = 1$, $(\hat{\pi} \cdot \widehat{B}) = 0$ and $(\hat{k}_0 \cdot \widehat{B}) = 0$. Again, $\boldsymbol{\mathcal{F}}^{\mathrm{n}}(\omega)$ and consequently $\boldsymbol{\mathcal{T}}(\omega)$ becomes diagonal and $\mathbf{A}'(\omega)$ is proportional to $T_{\sigma\sigma}(\omega)$, but depends now on $F_{\pm 1}$. This is a situation where the $F_{\pm 1}$-transitions are excited, and $\mathbf{A}'(\omega)$ results in

$$\mathbf{A}'(\omega) = \mathrm{e}^{-\mu_{\mathrm{e}} L/2} \begin{bmatrix} 1 \\ 0 \end{bmatrix} \mathrm{e}^{(3/4)\mathrm{i}\chi(1/(\Delta_1 - \mathrm{i}) + 1/(3(\Delta_4 - \mathrm{i})) + 1/(\Delta_6 - \mathrm{i}) + 1/(3(\Delta_3 - \mathrm{i})))}. \tag{3.7}$$

This is a more complex geometry, since now four sublevels with two different transition strengths contribute to $\mathbf{A}'(\omega)$. The two strongest transitions (1 and 6), which at room temperature are separated by $\hbar\delta\omega_{6,1} = 109.8\,\Gamma$, lead to the dominating beating with a beat period of $T \simeq 8$ ns. In addition, the resulting time spectrum contains interference

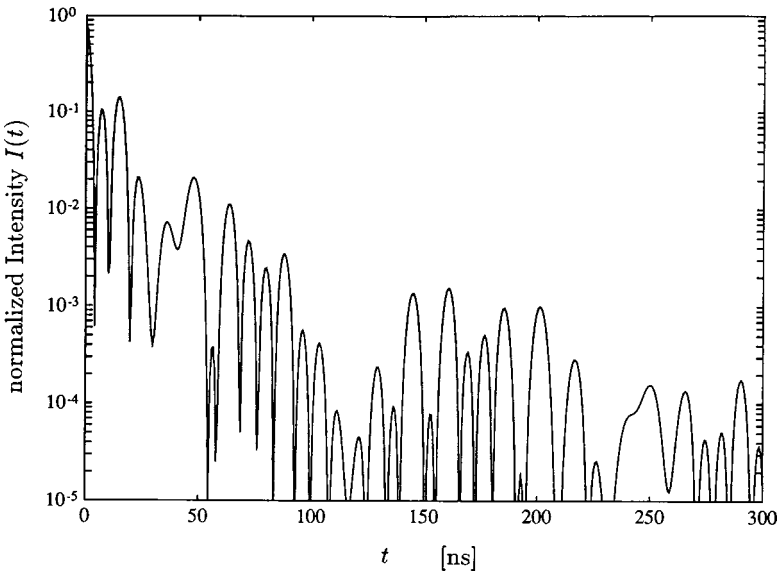

Figure 11. Delayed intensity $I(t)$ at room temperature for the geometry $\widehat{B} \parallel \widehat{\sigma}$ with an effective thickness $\chi = 40$.

from the other lines and, for large χ's, a superposition of different non-exponential envelopes. The resulting room temperature spectrum $I(t)$ for $\chi = 40$ is shown in figure 11. Figure 11 shows that the 8 ns beat period dominates the rather complicated time spectrum. A simple separation of contributions resulting from hyperfine splitting and speedup as in figure 9 is no longer possible. If the hyperfine splitting is only due to a **B**-field, the information contained in the spectra shown in figures 9 and 11 is identical. If, on the other hand, the ^{57}Fe nuclei are located in sites with different magnitudes of B and/or if an additional field is acting on the nucleus, the two geometries provide different information.

The two geometries $\widehat{B} \parallel \widehat{\sigma}$ and $\widehat{B} \parallel \hat{\pi}$ result in a diagonal transmission amplitude $\boldsymbol{\mathcal{T}}(\omega)$. Therefore a photon which is in a state of σ-polarization, remains σ-polarized when it is forward scattered. Any other direction of the **B**-field leads to a polarization mixing, which is the central theme of our chapter.

3.4. $\widehat{B} \parallel \hat{k}_0$ (Faraday geometry)

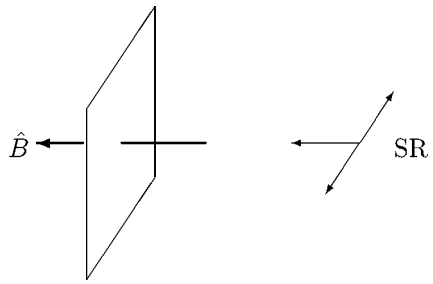

The "cleanest" geometry in which polarization mixing can occur is achieved when $\widehat{B}$ is parallel to $\hat{k}_0$. In optics this geometry is known as the Faraday geometry. However, as discussed further on in this section, one has to be careful with an analogy since the polarization mixing resulting from NFS is different from the conventional Faraday effect. The Faraday geometry results in $(\widehat{\sigma} \cdot \widehat{B}) = 0$, $(\hat{\pi} \cdot \widehat{B}) = 0$ and $(\hat{k}_0 \cdot \widehat{B}) = 1$. $\boldsymbol{\mathcal{F}}^{\mathrm{n}}(\omega)$ is not diagonal and all four matrix elements depend on $F_{\pm 1}$. The transmitted amplitude of an incident σ-polarized wave depends now on the matrix elements $T_{\sigma\sigma}(\omega)$ and $T_{\pi\sigma}(\omega)$ (as seen in eq. (2.35)). The resulting $\mathbf{A}'(\omega)$ is given by

$$\mathbf{A}'(\omega) = \mathrm{e}^{-\mu_{\mathrm{e}} L/2} \left\{ \frac{1}{2} \begin{bmatrix} 1 \\ 0 \end{bmatrix} \left(\mathrm{e}^{(3/2)\mathrm{i}\chi(1/(\Delta_1 - \mathrm{i}) + 1/(3(\Delta_4 - \mathrm{i}))} + \mathrm{e}^{(3/2)\mathrm{i}\chi(1/(\Delta_6 - \mathrm{i}) + 1/(3(\Delta_3 - \mathrm{i})))} \right) \right.$$
$$\left. + \frac{\mathrm{i}}{2} \begin{bmatrix} 0 \\ 1 \end{bmatrix} \left(\mathrm{e}^{(3/2)\mathrm{i}\chi(1/(\Delta_1 - \mathrm{i}) + 1/(3(\Delta_4 - \mathrm{i})))} - \mathrm{e}^{(3/2)\mathrm{i}\chi(1/(\Delta_6 - \mathrm{i}) + 1/(3(\Delta_3 - \mathrm{i})))} \right) \right\}, \quad (3.8)$$

where the first term corresponds to the unrotated σ-component $T_{\sigma\sigma}(\omega)$ and the second term to the 90° rotated π-component $T_{\pi\sigma}(\omega)$. The rotation of polarization of an incident σ-polarized beam as a function of time is illustrated in figure 12, where $\mathbf{A}'(t)$

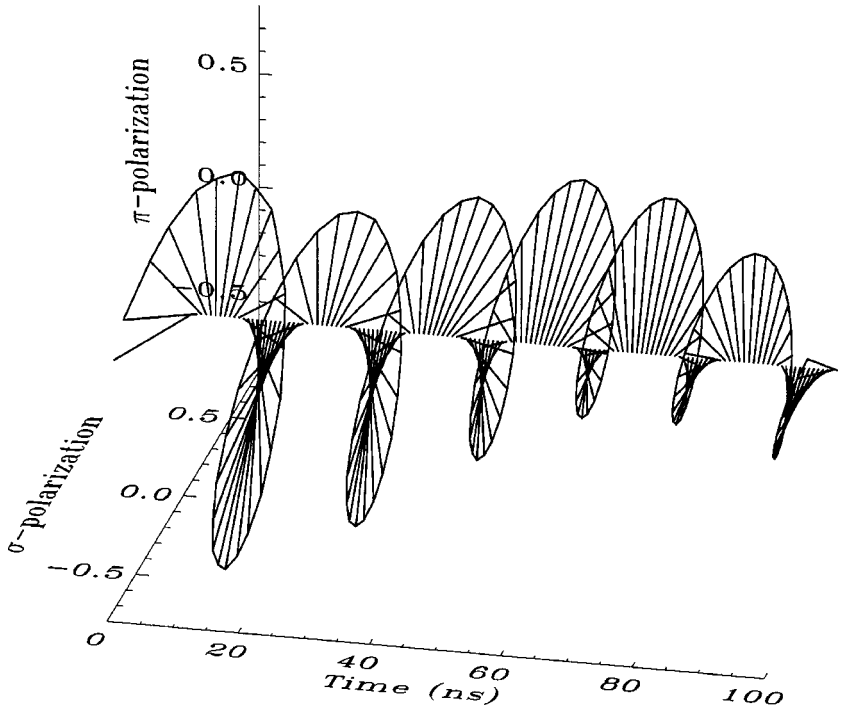

Figure 12. $\mathbf{A}'(t)$ for $\widehat{B} \parallel \hat{k}_0$ and $\chi = 2$ at room temperature.

is shown. To avoid unnecessary complications from modulation in the envelope, a moderate value of $\chi = 2$ is chosen.

As can be seen in figure 12 at $t = 0$ the polarization is that of the incident beam, and one full rotation occurs every 14 ns. This is the beat period resulting from $\delta\omega_{4,1}$ and $\delta\omega_{6,3}$, which each correspond to a pair of transitions with the same circular polarization (see figure 3). To characterize this state of polarization it is useful to compare the time of a full rotation (14 ns) with the time of one oscillation at 14.4 keV ($2.7 \cdot 10^{-19}$ s). In other words, it takes $5 \cdot 10^{10}$ oscillations to rotate the polarization by 360°.

Hence, the polarization is essentially linear, rotating "very slowly" in time. For a decreasing **B**-field the time for a rotation gets longer and eventually the polarization remains purely linear in the σ-state. In this case $T_{\pi\sigma}(\omega) = 0$ and eq. (3.8) turns into eq. (3.3). In figure 13 the total intensity $I(t)$ and the two polarization components $I_{\sigma\sigma}(t)$ and $I_{\pi\sigma}(t)$ are shown. As can be seen, $I(t)$ has a modulation with a beat period of 14 ns. Since the left and right circular polarization states are orthogonal to each other, there is no interference between them. The fact that the minima in $I(t)$ do not go to zero arises from the different Clebsch–Gordan coefficients for transition 1 compared to 4, and 3 compared to 6. The components $I_{\sigma\sigma}(t)$ and $I_{\pi\sigma}(t)$ show a beating with half the beat period, reflecting the rotation projected into a linear base. As a consequence, $I_{\pi\sigma}(t) = 0$ at $t = 0$, and initially the polarization is unrotated. Following eq. (2.37) $I_{\pi\sigma}(t)$ can be separated out, by adding a crossed π-polarizer downstream of the resonant

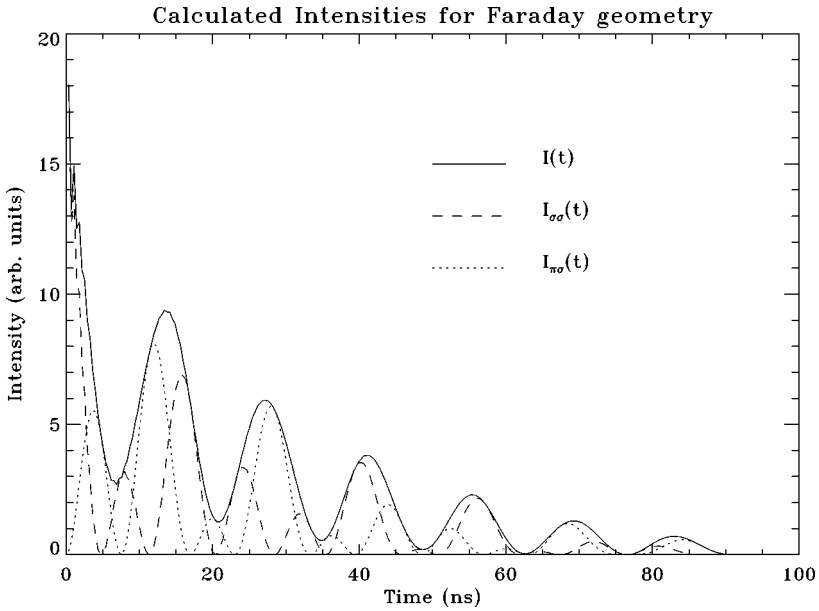

Figure 13. $I(t)$, $I_{\sigma\sigma}(t)$ and $I_{\pi\sigma}(t)$ with $\widehat{B} \parallel \hat{k}_0$ and $\chi = 2$.

scatterer. Then, only the second term of eq. (3.8) determines the total intensity and $I(t) = I_{\pi\sigma}(t)$. Figure 2 shows the apparatus used to demonstrate the effects described above.

Experimental data demonstrating this behavior is shown in figure 14, taken from [8]. The sample was inserted into the polarized X-ray beam such that it could be polarized as closely as possible with B parallel to k. Since it is notoriously difficult to magnetically polarize a thin foil perpendicular to its plane, we were forced to place the sample as closely as possible to be parallel to the X-ray beam. We were able to bring it to an angle of 17° before normal X-ray absorption reduced the intensity excessively. This geometry resulted in predominantly Faraday-type behavior. In contrast to NFS without crossed polarizer, where the first 20 ns are contaminated from the tail of prompt scattering, we are now able to follow the evolution from zero time, since the heavy overload is completely eliminated. It shows that this component of intensity starts out at zero, indicating that, initially, the transmitted wave is unrotated, and that its polarization rotates as time progresses due to the changing phases of the circularly polarized components.

It is interesting to consider an incident beam with circular polarization. In this case, one has to include the other two matrix elements $T_{\pi\pi}(\omega) = T_{\sigma\sigma}(\omega)$ and $T_{\sigma\pi}(\omega) = -T_{\pi\sigma}(\omega)$ to calculate the scattering, and it is easy to show that a right circular polarized incident beam ($\mathbf{A}(\omega) = (1/\sqrt{2})[1, \mathrm{i}]$) only excites the right circular transitions 1 and 4. The transmitted amplitude $\mathbf{A}'(\omega)$ only contains $F_1(\omega)$, and the polarization of the scattered radiation remains right circular polarized. Similarly, a left circular polarized incident wave given by $\mathbf{A}(\omega) = (1/\sqrt{2})[1, -\mathrm{i}]$ only excites

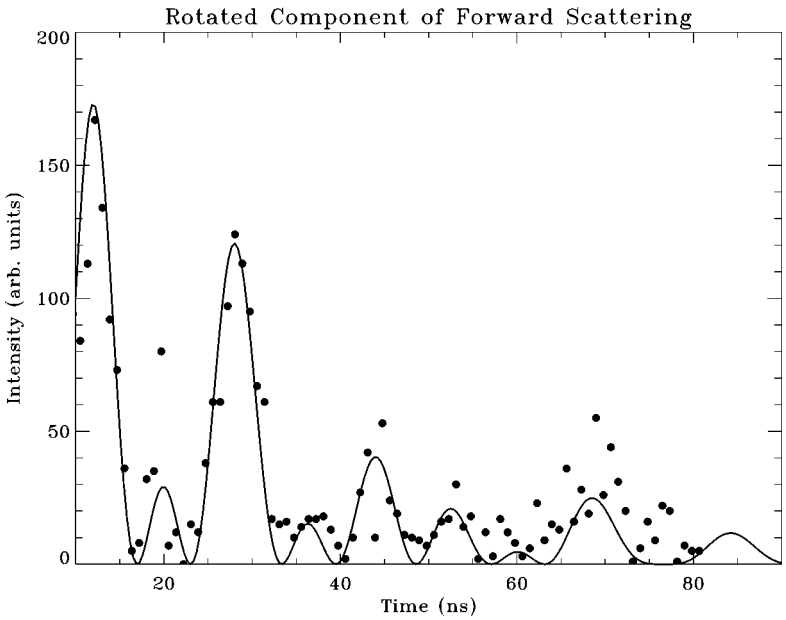

Figure 14. Intensity component $I_{\pi\sigma}(t)$ for the geometry $\widehat{B}$ approximately parallel to $\hat{k}_0$, an effective sample thickness of 1.6 μm and room temperature splittings.

the $\Delta m = -1$-transitions. Circular polarization states are eigenstates for the Faraday geometry, and remain unaffected.

3.4.1. Comparison of NFS in the Faraday geometry with the optical Faraday effect

For a comparison of polarization mixing resulting from NFS in the Faraday geometry with the optical Faraday effect, $\mathbf{A}'(t)$ is shown for two sample thicknesses L which correspond to $\chi = 1$ and $\chi = 3$.

A magnetic field of $B = 20$ T acting on the nucleus is assumed for the calculations in figure 15. As can be seen in the figure a change of χ (and therefore the sample thickness L) only affects the speedup, but not the rotation of the polarization. This result is surprising when compared to the conventional Faraday effect, where the rotation of polarization is proportional to L.

In the simplest picture the optical Faraday effect can be described as follows. The rotating **E**-field of a quasi monochromatic circular polarized incident wave with frequency ω forces an elastically bound electron on a steady-state circular orbit. The application of a large **B**-field perpendicular to the orbit plane (parallel to $\hat{k}_0$) results in a radial force of magnitude $F = (Be\omega r)$, where r is the radius of the orbit. The force can point either towards or away from the orbit's center, depending on the polarization and **B**-field direction. Consequently the total radial force on the electron (F plus the elastic restoring forces) results in a new radius r' depending on the handedness of the polarization and the direction and magnitude of **B**. This leads to two different values for the electric dipole moment and hence for the index of refraction. The

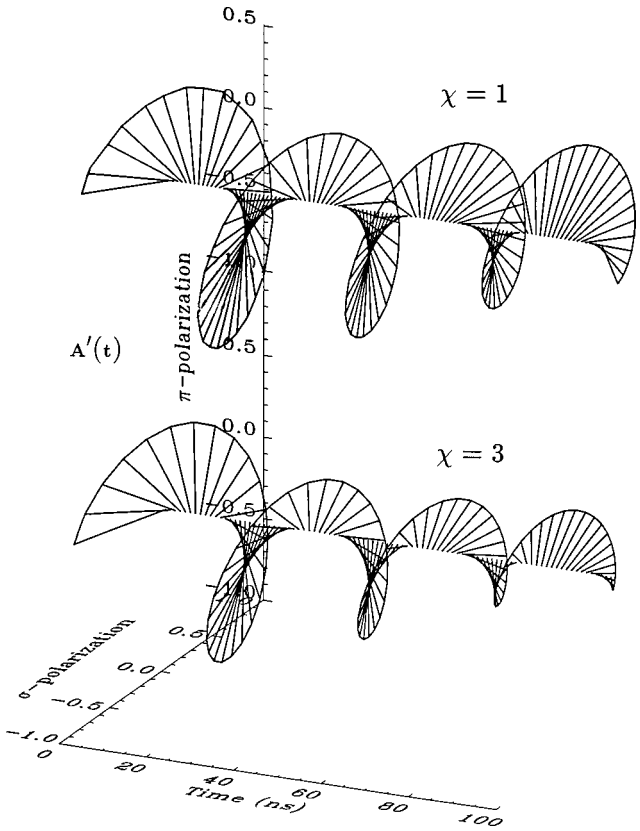

Figure 15. $\mathbf{A}'(t)$ with $\widehat{B} \parallel \hat{k}_0$ for $\chi = 1$ and $\chi = 3$. A **B**-field of 20 T is acting on the nucleus. In contrast to the conventional Faraday effect, the rotation is unaffected by the change in thickness.

difference is proportional to B and depends further on the magnitude of the restoring force compared to F. If $\tilde{n}(\omega)$ is expressed as a 2×2 matrix in a linear basis only the off diagonal matrix elements are affected and $\tilde{n}(\omega)$ can be written as

$$\tilde{n}(\omega) = \tilde{\mathbf{1}} + \lambda \begin{bmatrix} z & -\mathrm{i}\mathcal{V}B \\ \mathrm{i}\mathcal{V}B & z \end{bmatrix}, \tag{3.9}$$

where z corresponds to the average phase shift and to absorption. $\mathcal{V}$ is called the Verdet constant and is dependent on the restoring forces acting on the electrons. It is usually determined empirically and is typically of order 10^{-6} min of arc T^{-1} cm^{-1} for solids. The opposite signs in the two off diagonal elements indicate the opposite effects on the two circular polarizations. Application of the formalism derived in section 2 to the new $\tilde{n}(\omega)$ from eq. (3.9) results in a transmission matrix

$$\mathcal{T}(\omega) = \mathrm{e}^{\mathrm{i}k_0\bar{n}L} \begin{bmatrix} \cos(\mathcal{V}BL) & -\sin(\mathcal{V}BL) \\ \sin(\mathcal{V}BL) & \cos(\mathcal{V}BL) \end{bmatrix}, \tag{3.10}$$

where $\bar{n} = 1 + \lambda z$ is the average index of refraction. An incident σ-polarized wave is transmitted as

$$\mathbf{A}' = \mathrm{e}^{\mathrm{i}k_0\bar{n}L} \begin{bmatrix} \cos(\beta) \\ \sin(\beta) \end{bmatrix} = \begin{bmatrix} \cos(\beta) & -\sin(\beta) \\ \sin(\beta) & \cos(\beta) \end{bmatrix} \begin{bmatrix} 1 \\ 0 \end{bmatrix} \tag{3.11}$$

and therefore rotated by an angle $\beta = \mathcal{V}\,B\,L$. An incident circular polarized wave ($\mathbf{A} = (1/\sqrt{2})[1, \pm\mathrm{i}]$) does not change its polarization, but experiences an additional phase shift of $\exp(\mp\mathrm{i}\beta)$, depending on the polarization. This results in the two indices of refraction $n_{\mathcal{R}} = \bar{n} - \lambda\mathcal{V}B$ for right circular polarized light and $n_{\mathcal{L}} = \bar{n} + \lambda\mathcal{V}B$ for left circular polarized light. The result shows that the rotation angle β is proportional to B and L and, further, the polarization is time-independent, remaining purely linear in its new orientation.

The reason for the difference lies in the frequency dependence of $\tilde{n}(\omega)$. In both NFS and the optical Faraday effect the assumption that the incident wave is quasi monochromatic ($|(\Delta\omega/\omega)| = |(\Delta\lambda/\lambda)| \ll 1$) and, therefore, $\lambda \simeq$ const is realistic. Using the model given above it then follows that $\mathcal{F}(\omega) =$ const. Obviously this approximation is not valid for NFS, where the energy width of even a *very* monochromatic wave with $|(\Delta\omega/\omega)| = 10^{-10}$ easily spans all four resonances involved in the scattering. Furthermore, the approximation $\mathcal{F} =$ const shows that in the optical Faraday effect for an incident short pulse, $\mathbf{A}'(t)$ remains a δ-function; the polarization is measured time integrated. This is the important difference between NFS and most other transmission measurements where the scattering is "fast" and the measured intensity is $I \simeq \int_0^\infty I(t)\,\mathrm{d}t$. A time integrated measurement probes the refracted (incident *plus* forward scattered) wave whereas NFS is a rather unique example where it is possible to separate out the forward scattered wave. In particular, the rotation of the polarization plane is driven by the frequency differences between the component waves, which is independent of the sample thickness, and so the rotation is thickness-independent. Thickness variations serve only to change the decay envelope of the collective decay process.

3.5. *σ-polarized beam with $\widehat{B} \perp \hat{k}_0$ and angle ϕ between $\widehat{B}$ and $\widehat{\sigma}$*

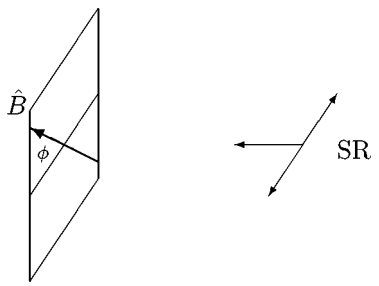

As already discussed, the two special cases of this geometry $\widehat{B} \parallel \hat{\pi}$ and $\widehat{B} \parallel \widehat{\sigma}$ do not result in polarization mixing. Any other direction of **B** in the $\widehat{\sigma}\hat{\pi}$-plane, however,

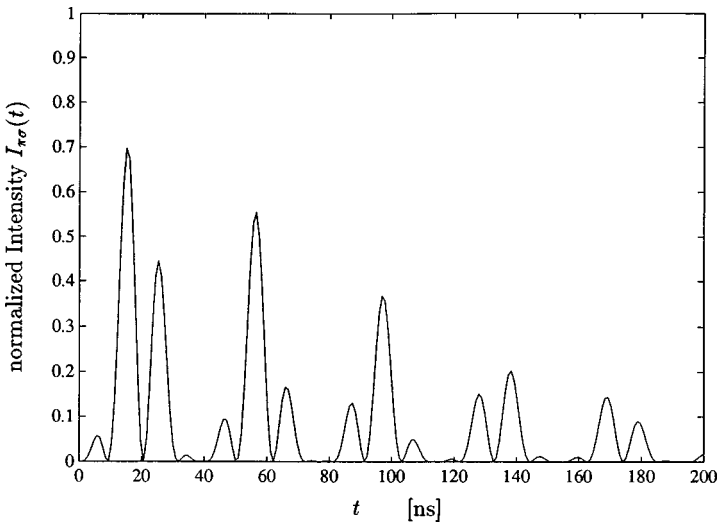

Figure 16. Intensity component $I_{\pi\sigma}(t)$ for the geometry $\widehat{B} \perp \hat{k}_0$ and $\chi = 1$ for room temperature splittings.

leads to a rotated component $T_{\pi\sigma}(\omega) = T_{\sigma\pi} \neq 0$. The resulting transmitted amplitude $\mathbf{A}'(\omega)$ has a rather complex form. Of particular interest is the situation when a crossed polarizer is added and only the rotated component $T_{\pi\sigma}(\omega)$ is separated out. Then $\mathbf{A}'(\omega)$ results in

$$\mathbf{A}'(\omega) = \mathrm{e}^{-\mu_\mathrm{e} L/2} \begin{bmatrix} 0 \\ 1 \end{bmatrix} \frac{\sin(2\phi)}{2} \Big\{ \mathrm{e}^{(3/4)\mathrm{i}\chi(1/(\Delta_1-\mathrm{i})+1/(3(\Delta_4-\mathrm{i}))+1/(\Delta_6-\mathrm{i})+1/(3(\Delta_3-\mathrm{i})))} - \mathrm{e}^{(3/2)\mathrm{i}\chi(2/(3(\Delta_2-\mathrm{i}))+2/(3(\Delta_5-\mathrm{i})))} \Big\} \tag{3.12}$$

with the angle ϕ shown in the figure. $\mathbf{A}'(\omega)$ scales like $\sin(2\phi)$ and reaches its maximum at $\phi = 45^\circ$. The important feature of this geometry is that $\mathbf{A}'(\omega)$ is, except for this scaling factor, independent of ϕ. Therefore, for a given magnitude of B any non-isotropic **B**-field distribution in a plane perpendicular to k_0 leads to an identical time spectrum. The technique of crossed polarizers applied in this geometry is, therefore, useful to determine the magnitude of the hyperfine splittings for any anisotropic **B**-field distribution perpendicular to k_0. Figure 16 shows $I_{\pi\sigma}(t)$ for $\chi = 1$. The time spectrum reflects interference due to all six lines and starts, as in the Faraday geometry, with $I(0) = 0$.

The unrotated component $I_{\sigma\sigma}(t)$ and the total intensity $I(t) = I_{\sigma\sigma}(t) + I_{\pi\sigma}(t)$ of this geometry have a slightly more complex dependence on ϕ. A measurement of the total intensity $I(t) = I_{\sigma\sigma}(t) + I_{\pi\sigma}(t)$ for the $\phi = 45^\circ$ case is also shown in figure 17, and of the rotated component $I_{\pi\sigma}(t)$ is shown in figure 18 [18].

Using the beryllium crystal as an analyzer has the advantage that it is quite transparent, and so one can measure the intensity transmitted through it while it is in

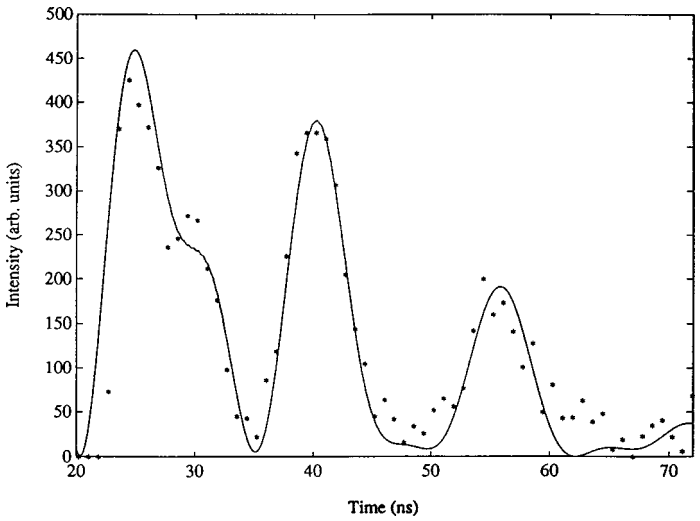

Figure 17. Measured total intensity $I(t) = I_{\sigma\sigma}(t) + I_{\pi\sigma}(t)$ for the geometry $\widehat{B} \perp \hat{k}_0$ and $\chi = 6.6$ for room temperature splittings. The solid line is a calculation.

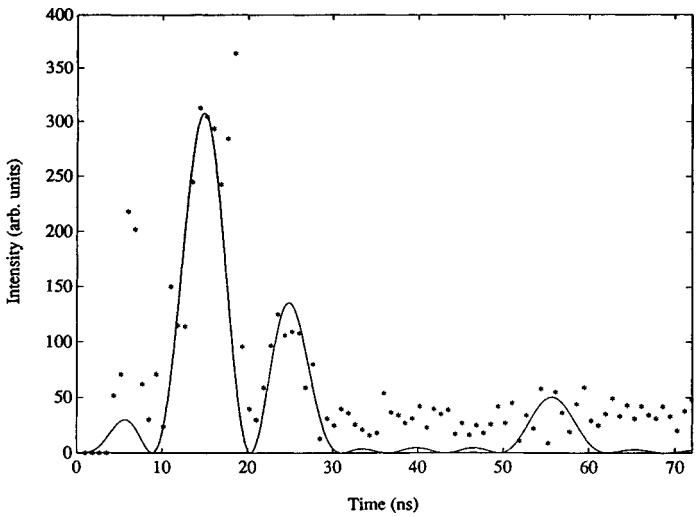

Figure 18. Measured intensity component $I_{\pi\sigma}(t)$ for the geometry $\widehat{B} \perp \hat{k}_0$ and $\chi = 6.6$ for room temperature splittings. The solid line is a calculation.

the Bragg condition. The Bragg reflection diverts some of the $I_{\pi\sigma}(t)$ and allows the rest of the intensity to pass (with some absorption). Figure 19 shows the result of this measurement. The measured data can be interpreted as being due to a mixture consisting of $I(t) = I_{\sigma\sigma}(t) + 0.5I_{\pi\sigma}(t)$, implying that the reflectivity of our analyzer is roughly 50%.

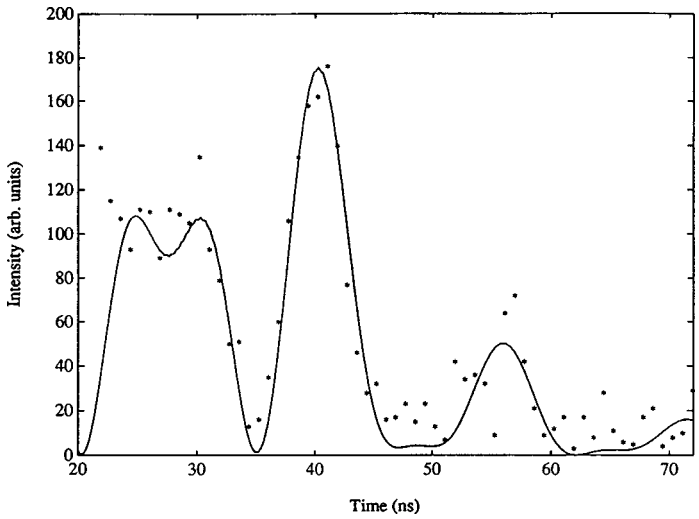

Figure 19. Measured intensity behind the beryllium analyzer crystal when it is set to reflect away part of the $I_{\pi\sigma}(t)$. The best agreement with calculation is found by assuming $I(t) = I_{\sigma\sigma}(t) + 0.5I_{\pi\sigma}(t)$.

3.6. Several samples

So far, different scattering geometries for just one sample with a well defined **B**-field were discussed. As already mentioned, the derived formalism applies to any number of samples and/or polarizers. If n samples are located in line, the transmission matrix $\boldsymbol{\mathcal{T}}_{\text{tot}}(\omega)$ corresponding to this array is given by

$$\boldsymbol{\mathcal{T}}_{\text{tot}}(\omega) = \boldsymbol{\mathcal{T}}_n(\omega)\cdots\boldsymbol{\mathcal{T}}_2(\omega)\boldsymbol{\mathcal{T}}_1(\omega). \tag{3.13}$$

If all n samples have identical splittings and their **B**-fields are oriented in the same direction, it can be easily shown that $\boldsymbol{\mathcal{T}}_{\text{tot}}(\omega)$ corresponds to $\boldsymbol{\mathcal{T}}(\omega)$ for one sample with effective thickness $\chi_{tot} = \chi_1 + \chi_2 + \cdots + \chi_n$. It is important to note that this is independent of the separation distance between the samples. The reason for this is that back reflections at the sample boundaries are negligible, and the wave traveling between the sample is not dispersed.

If either the magnitude or the direction of the **B**-field varies from sample to sample the resulting $\boldsymbol{\mathcal{T}}_{\text{tot}}(\omega)$ becomes more complex. Three examples of NFS from two subsequent identical samples with different **B**-field directions are briefly discussed. The first is shown in figure 20. As a first guess one might think that $\boldsymbol{\mathcal{T}}_{\text{tot}}(\omega)$ is similar for both geometries, since the orientation of the **B**-field in geometry (b) can be achieved by applying two orthogonal **B**-fields as shown in geometry (a). However, a look at the appropriate transmission amplitudes immediately reveals the difference. Geometry (a) is characterized by a $\boldsymbol{\mathcal{T}}_{\text{tot}}(\omega)$ which is diagonal since, as discussed in the previous sections, $\boldsymbol{\mathcal{T}}_1(\omega)$ and $\boldsymbol{\mathcal{T}}_2(\omega)$ are diagonal. In geometry (b), however, $\boldsymbol{\mathcal{T}}_{\text{tot}}(\omega)$ contains off-diagonal elements $T_{\pi\sigma_{\text{tot}}}(\omega) = T_{\sigma\pi_{\text{tot}}}(\omega) \neq 0$ as given in eq. (3.12) with $\chi = \chi_1 + \chi_2$. As a result the polarization shows, unlike in geometry (a), a mixing. A comparison of

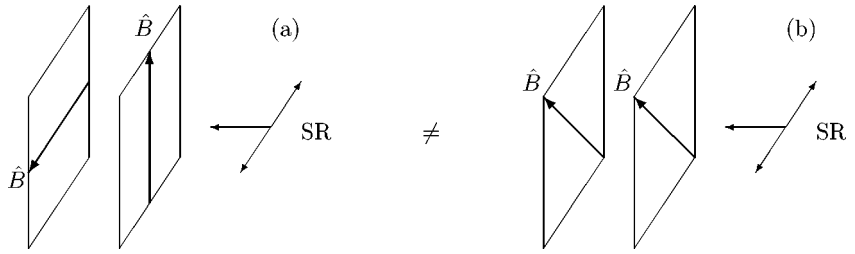

Figure 20. Comparison of two "similar" sample geometries. In geometry (a) $\widehat{B} \parallel \hat{\pi}$ and $\widehat{B} \parallel \widehat{\sigma}$, respectively. In geometry (b) $\phi = 45^\circ$.

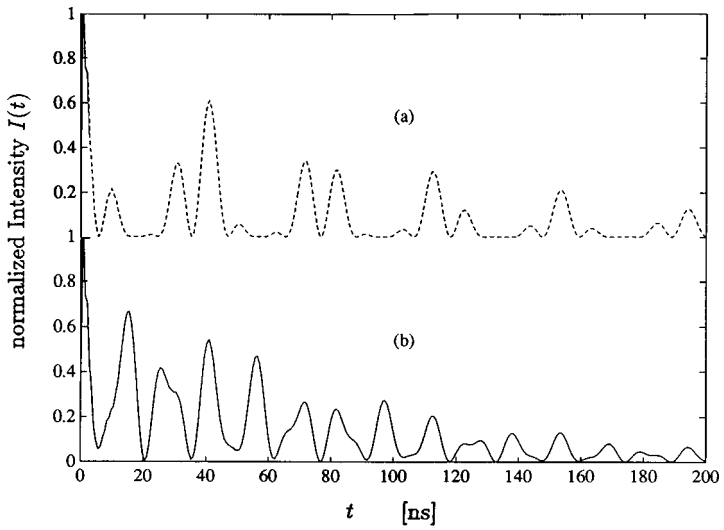

Figure 21. Comparison of NFS from two subsequent samples. The dotted line shows $I(t)$ for geometry (a) and the solid line shows $I(t)$ for geometry (b) in figure 20. The effective thicknesses are $\chi_1 = \chi_2 = 1$, and room temperature splitting is assumed.

the total intensities $I(t)$ for the two geometries is shown in figure 21. Comparison of the intensities for the two geometries shown in figure 22, on the other hand, leads to identical results for $I(t)$. Even though in geometry (c) each sample is characterized by a $\boldsymbol{\mathcal{T}}(\omega)$ which includes off diagonal matrix elements, $T_{\pi\sigma_{\rm tot}} = T_{\sigma\pi_{\rm tot}}(\omega) = 0$. This is true for any two orthogonal **B**-field directions perpendicular to $\hat{k}_0$. The intensity $I(t)$ for geometry (c) is therefore also given by the dotted line in figure 21.

In a conventional Mössbauer experiment energy shifts, such as isomer or temperature shifts, move the absorption minimum from the center at zero velocity. Since, unlike a conventional source, the broad SR pulse does not provide a well defined reference energy, such shifts do not affect the time spectrum of NFS. If, however, two samples, in which different energy shifts occur, are located behind each other, one acts as a reference, and the shifts affect the resulting time spectrum. An example for this is the second order Doppler shift, which arises when two samples have different

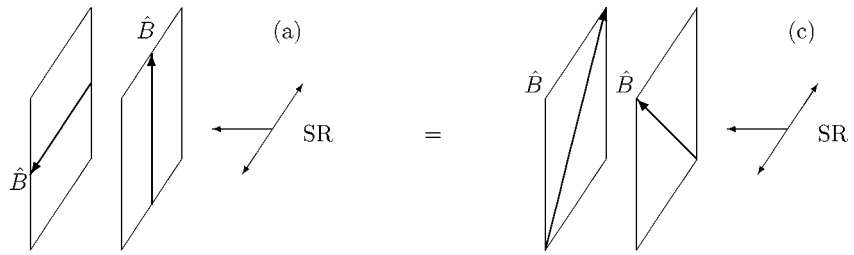

Figure 22. Comparison of NFS from two samples with perpendicular **B**-fields.

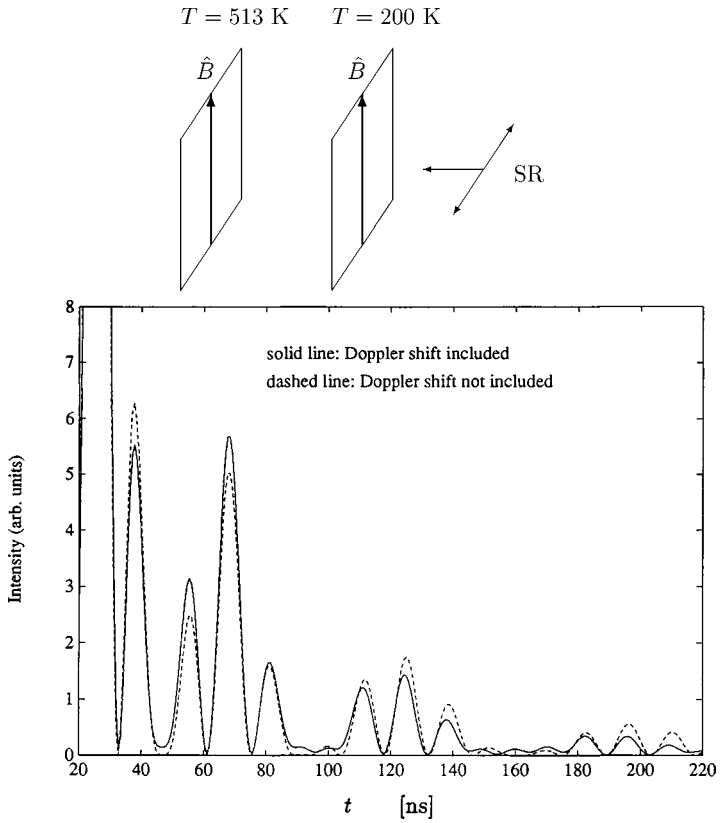

Figure 23. NFS from two samples at different temperatures. The calculations show the effect of the second order Doppler shift on the time spectrum.

temperatures. Figure 23 shows a possible geometry to measure the temperature shift, and the corresponding time spectra. In the calculation a thickness $L = 10$ μm and a ^{57}Fe abundance of $p = 0.95$ are assumed for both samples. The values for f_{LM} and the splitting at 200 K and 513 K are those experimentally obtained (see [17]). The Doppler shift is calculated by assuming the classical limit, which for Fe results in $\delta\omega/\delta T = -2.44 \cdot 10^{-15}\omega$ per K [42] corresponding to a relative shift of $2.36\,\Gamma$ for

$\Delta T = 313$ K. The comparison of the two calculations shows the effect of the second order Doppler shift on the time evolution. The relative weight of the quantum beat maxima is changed due to the additional frequency introduced by the Doppler shift. The quality of the time spectra obtained in [17] indicates that shifts of a small fraction of Γ should be easily observable in NFS experiments at NSLS. At third generation SR sources much smaller energy shifts will be observable. Furthermore, due to the high collimation of the SR beam, two samples can be separated by a large distance with essentially no loss in intensity. It might therefore be possible to do a measurement of the gravitational shift á la Pound and Rebka [23] with improved precision.

4. Summary

The ability to separate in time the scattered radiation from the excitation pulse provides a rich variety of unusual polarized scattering phenomena. A large number of geometries is possible, which can be applied to detect small energy shifts, separate certain sample parameters, or demonstrate optical and other phenomena related to the Mössbauer effect. The intrinsic polarization of the SR beam and/or the use of additional polarizers or interferometers makes such phenomena readily accessible to the experimenter. In this paper we have developed the formalism to calculate polarization phenomena in NFS. For illustration we have calculated several spectra resulting from relatively simple geometries. We have, furthermore, shown early results which were in good agreement with theory. With the advent of third generation SR sources and adequately optimized optics the study of polarization phenomena can be extended to dilute systems. Finally, SR beams with neV-resolution can be produced at intensities of 10^3 to 10^5 photons/s. Much remains to be studied in this area, and we hope we will stimulate further activities of this type.

References

[1] G. Schütz, W. Wagner, W. Wilhelm, P. Kienle, R. Zeller, R. Frahm and G. Materlik, Phys. Rev. Lett. 58 (1987) 737.
[2] M. Blume and O.C. Kistner, Phys. Rev. 171 (1968) 417.
[3] E. Hecht, *Optics*, 2nd ed. (Addison-Wesley, Reading, MA, 1989).
[4] M. Hart, Philos. Mag. B 38 (1978) 41.
[5] U. Bonse and M. Hart, Appl. Phys. Lett. 7 (1965) 238.
[6] M. Hart and A.R.D. Rodrigues, Philos. Mag. B 40 (1979) 149.
[7] D.P. Siddons, M. Hart, Y. Amemiya and J.B. Hastings, Phys. Rev. Lett. 64 (1990) 1967.
[8] D.P. Siddons, U. Bergmann and J.B. Hastings, Phys. Rev. Lett. 70 (1993) 359.
[9] D.P. Siddons, J.B. Hastings, U. Bergmann, F. Sette and M. Krisch, Nucl. Instrum. Methods B 103 (1995) 371.
[10] T.S. Toellner, E.E. Alp, W. Sturhahn, T.M. Mooney, X. Xhang, M. Ando, Y. Yoda and S. Kikuta, Appl. Phys. Lett. 67 (1995) 1993.
[11] J.P. Hannon and G.T. Trammell, Phys. Rev. 186 (1969) 306.
[12] Yu. Kagan and A.M. Afanas'ev, Z. Naturforsch. 28a (1973) 1351.

[13] J.D. Jackson, *Classical Electrodynamics*, 2nd ed. (Wiley, New York, 1975).
[14] J.P. Hannon, N.J. Carron and G.T. Trammell, Phys. Rev. B 9 (1974) 2810.
[15] J.P. Hannon, private communication.
[16] J.G. Stevens and V.E. Stevens, *Mössbauer Effect Data Index* (IFI/Plenum, ISBN-0-306-65146-7, 1975).
[17] U. Bergmann, S.D. Shastri, D.P. Siddons, B.W. Batterman and J.B. Hastings, Phys. Rev. B 50 (1994) 5957.
[18] U. Bergmann, D.P. Siddons and J.B. Hastings, Hyp. Interact. 92 (1994) 1113.
[19] Yu. Kagan, A.M. Afanas'ev and V.G. Kohn, J. Phys. C 12 (1979) 615.
[20] J.B. Hastings, D.P. Siddons, U. van Bürck, R. Hollatz and U. Bergmann, Phys. Rev. Lett. 66 (1991) 770.
[21] U. van Bürck, D.P. Siddons, J.B. Hastings, U. Bergmann and R. Hollatz, Phys. Rev. B 46 (1992) 6207.
[22] F.J. Lynch, R.E. Holland and M. Hammermesh, Phys. Rev. 120 (1960) 513.
[23] R.V. Pound and G.A. Rebka, Jr., Phys. Rev. Lett. 4 (1960) 337.
[24] P.B. Moon, Proc. Phys. Soc. London A 64 (1951) 76.
[25] K.G. Malmfors, Ark. Fysik 6 (1952) 49.
[26] R.L. Mössbauer, Z. Physik 151 (1958) 124.
[27] R.L. Mössbauer, Naturwissenschaften 45 (1958) 538.
[28] W.E. Lamb, Phys. Rev. 55 (1939) 190.
[29] H. Frauenfelder, *The Mössbauer Effect* (Benjamin, New York, 1963).
[30] E.J. Seppi and F. Boehm, Phys. Rev. Lett. 128 (1962) 2334.
[31] H. Winick and S. Doniach, *Synchrotron Radiation Research* (Plenum, New York, 1980).
[32] S.L. Ruby, J. Phys. Colloq. (Paris) 35 (1974) C6-209.
[33] R.L. Cohen, G.L. Miller and K.W. West, Phys. Rev. Lett. 41 (1978) 381.
[34] E. Gerdau, R. Rüffer, H. Winkler, W. Tolksdorf, C.P. Klages and J.P. Hannon, Phys. Rev. Lett. 54 (1985) 835.
[35] E. Gerdau, R. Rüffer, R. Hollatz and J.P. Hannon, Phys. Rev. Lett. 57 (1986) 1141.
[36] G.T. Trammell and J.P. Hannon, Phys. Rev. B 18 (1978) 165, and 19 (1979) 3835.
[37] G. Faigel, D.P. Siddons, J.B. Hastings, P.E. Haustein, J.R. Grover, J.P. Remeika and A.S. Cooper, Phys. Rev. Lett. 58 (1987) 2699.
[38] U. van Bürck, R.L. Mössbauer, E. Gerdau, R. Rüffer, R. Hollatz, G.V. Smirnov and J.P. Hannon, Phys. Rev. Lett. 59 (1987) 355.
[39] J.B. Hastings, D.P. Siddons, G. Faigel, L.E. Berman P.E. Haustein and J.R. Grover, Phys. Rev. Lett. 63 (1989) 2252.
[40] S. Margulies and J.R. Ehrman, Nucl. Instrum. Methods 12 (1961) 131.
[41] S.D. Shastri, private communication.
[42] R.V. Pound and G.A. Rebka, Jr., Phys. Rev. Lett. 4 (1960) 274.
[43] M. Grote, R. Röhlsberger, M. Dimer, E. Gerdau, R. Hellmich, R. Hollatz, J. Jäschke, E. Lüken, J. Metge, R. Rüffer, H.D. Rüter, W. Sturhahn E. Witthoff, M. Harsdorff, W. Pfützner, M. Chambers and J.P. Hannon, Europhys. Lett. 17 (1991) 708.
[44] R. Röhlsberger, E. Gerdau, M. Harsdorff, O. Leupold, E. Lüken, J. Metge, R. Rüffer, H.D. Rüter, W. Sturhahn and E. Witthoff, Europhys. Lett. 18 (1992) 561.
[45] R. Röhlsberger, Ph.D. thesis, Hamburg (1994).
[46] B.W. Batterman and H. Cole, Rev. Modern Phys. 36 (1964) 681.
[47] L.E. Berman, J.B. Hastings, T. Oversluizen and M. Woodle, Rev. Sci. Instrum. 63 (1992) 428.
[48] J.W.M. DuMond, Phys. Rev. 52 (1937) 872.
[49] D.P. Siddons, J.B. Hastings, G. Faigel, L.E. Berman, P.E. Haustein and J.R. Grover, Phys. Rev. Lett. 62 (1989) 1384.

[50] E.E. Alp, T.M. Mooney, T. Toellner, W. Stuhrhahn, E. Witthoff, R. Röhlsberger, E. Gerdau, H. Homma and M. Kentjana, Phys. Rev. Lett. 70 (1993) 3351.
[51] W. Sturhahn, E. Gerdau, R. Hollatz, R. Rüffer, H.D. Rüter and W. Tolksdorf, Europhys. Lett. 14 (1991) 821.
[52] D.E. Johnson, D.P. Siddons and J.B. Hastings, Phys. Rev. B 51 (1995) 7909.